Atmos. Chem. Phys., 26, 12479–12503, 2026
https://doi.org/10.5194/acp-26-12479-2026

Atmospheric Chemistry and Physics
Open Access
EGU

Research article

Revisiting the critical role of stabilized Criegee intermediates (sCIs) in sulfuric acid formation: coupling mechanistic updates with interpretable machine learning

Yuhuan Zhu[1], Qiang Chen[1,2], Luyan He[1], Chunlin Shang[3], Li Jiang[4], Donghong Guan[4], Guirong Yao[4], and Wenkai Guo[5]

[1]Key Laboratory for Semi–Arid Climate Change of the Ministry of Education, College of Atmospheric Sciences, Lanzhou University, Lanzhou, 730000, China
[2]Lanzhou University Applied Technology Research Institute Co., Ltd, Lanzhou, 730000, China
[3]Inner Mongolia Autonomous Region Environmental Monitoring Center, Wuhai Branch, Wuhai, 016000, China
[4]Gansu Provincial Ecological and Environmental Engineering Assessment Center, Lanzhou 730000, China
[5]Faculty of Geosciences and Environmental Engineering, Southwest Jiaotong University, Chengdu, 611756, China

Correspondence: Qiang Chen (chenqqh@lzu.edu.cn)

Received: 16 December 2025 – Discussion started: 12 February 2026
Revised: 27 July 2026 – Accepted: 6 August 2026 – Published: 2 September 2026

Abstract. Sulfuric acid, formed via gas-phase SO_2 oxidation, drives new particle formation and secondary sulfate aerosol under low relative humidity (RH). Beyond the well-established OH-mediated pathway, stabilized Criegee intermediates (sCIs) from alkene ozonolysis provide an additional SO_2 oxidation route whose rate ($L_{SO_2,sCIs}$) and fractional contribution (μ_{sCIs}) vary markedly across environments. Although prior studies have documented this spatiotemporal heterogeneity, quantifying the individual factor contributions governing these differences remains lacking. Furthermore, because sCI and OH formation share common precursors yet differ mechanistically, μ_{sCIs} can alter the sensitivity of total SO_2 oxidation (L_{SO_2}) to precursor variations, but the magnitude of this influence remains unclear. Here, we updated Criegee-related reactions in MCM v3.3.1 following recent IUPAC recommendations, conducted extensive AtChem box-model simulations, and trained interpretable XGBoost surrogate models to attribute $L_{SO_2,sCIs}$ and μ_{sCIs} to their controlling factors and examine how μ_{sCIs} regimes modulate L_{SO_2} sensitivity. $L_{SO_2,sCIs}$ was primarily controlled by RH and isoprene. The dominant drivers of μ_{sCIs} differed between day and night: daytime factors included alkene speciation, O_3, and the alkene fraction in VOCs; nighttime factors included alkene speciation, RH, and NO_x. Under high-μ_{sCIs} regimes, positive L_{SO_2}responses to O_3, VOCs, and alkene fraction were consistently amplified relative to low-μ_{sCIs} regimes. Field observation-based modeling of a summer episode in Wuhai supported these regime-dependent patterns. These findings indicate that reducing VOC emissions provides a more effective mechanism for regulating sulfuric acid formation under conditions with active alkene ozonolysis.

Published by Copernicus Publications on behalf of the European Geosciences Union.

1 Introduction

The environmental and climatic impacts of fine particulate matter ($PM_{2.5}$) are strongly influenced by sulfate aerosol (SO_4^{2-}), which plays a key role in regulating aerosol acidity (Yao et al., 2018), hygroscopicity (Gunthe et al., 2011), and direct radiative forcing (Quaas et al., 2022). Although a minor fraction of particulate sulfate is directly emitted from anthropogenic sources such as coal and biomass combustion (Dai et al., 2019), industrial activities (Song et al., 2025), and transportation (Cao et al., 2025), it is formed predominantly from the atmospheric oxidation of sulfur dioxide (SO_2) via gas-phase, aqueous-phase, and heterogeneous pathways (Ye et al., 2023). During severe haze events, elevated relative humidity and aerosol loadings significantly enhance aqueous-phase and heterogeneous SO_2 oxidation. These multiphase processes dominate sulfate formation and have therefore been the focus of extensive mechanistic investigations (Cao et al., 2021). Nevertheless, the gas-phase oxidation of SO_2 remains critically important because its product, sulfuric acid (H_2SO_4), is a key precursor for atmospheric new particle formation (NPF). Atmospheric nucleation and the subsequent growth of newly formed particles represent a major source of aerosol particles in terms of number concentration, and NPF has been frequently observed even in highly polluted urban environments characterized by strong condensation sinks (Yao et al., 2018). Moreover, over the past decade, stringent emission-control policies in East Asia, particularly in China, have substantially reduced $PM_{2.5}$ concentrations (Geng et al., 2021), thereby weakening conditions favorable for aqueous-phase and heterogeneous sulfate formation. In this progressively cleaner atmosphere, the relative importance of gas-phase pathways is expected to increase (Wang et al., 2025). Therefore, under increasingly stringent air pollution control targets (WHO, 2021), the role of SO_2 gas-phase oxidation pathways in secondary aerosol production is expected to become more important and warrants further investigation.

Hydroxyl radicals (OH) have long been recognized as the dominant oxidant in gas-phase SO_2 oxidation. Since the pioneering work of Cox and Penkett (1971) first demonstrated that Criegee intermediates (CIs, zwitterionic carbonyl oxides) react with SO_2 in the gas phase, extensive laboratory and theoretical studies (Taatjes et al., 2013; Vereecken et al., 2012) have advanced understanding of the formation, stabilization, and fate of CIs. Stabilized Criegee intermediates (sCIs) are therefore increasingly considered an important complementary pathway for gas-phase SO_2 oxidation and a potentially significant contributor to H_2SO_4 formation. Multiple field observational studies conducted in the boreal forests in Finland (Mauldin et al., 2012), the SMEAR II station in Finland and the Hohenpeissenberg station in Germany (Boy et al., 2013), in urban Beijing (Guo et al., 2021), and at a remote Mediterranean site strongly influenced by biogenic VOC emissions (Kukui et al., 2021) suggest that sCIs can provide an additional, environment-dependent pathway for SO_2 oxidation. Notably, as the direct measurement of atmospheric sCIs concentrations remains a formidable challenge, observational studies have primarily relied on the analysis of precursors and OH radical concentrations to provide qualitative evidence. Consequently, numerical simulations grounded in CIs chemical kinetics are indispensable for quantifying the contribution of sCIs to the gas-phase SO_2 oxidation rate.

To date, numerical modeling studies have extensively evaluated the contribution of sCIs to SO_2 oxidation across a broad range of spatial scales and environmental conditions. For instance, utilizing a steady-state approximation, Khan et al. (2017) estimated that the OH-driven SO_2 oxidation rate in urban London ($0.64\,Tg\,yr^{-1}$) was approximately 17 times that of the sCI pathway ($37.6\,Gg\,yr^{-1}$). However, proxy calculations of H_2SO_4 concentrations have revealed pronounced regional disparities: at the semi-pristine boreal forest site in Hyytiälä, the photochemical pathway ($SO_2 + OH$) and the alkene ozonolysis pathway (SO_2 + sCIs) accounted for approximately 34 % and 60 % of H_2SO_4 production, respectively, whereas in heavily polluted Beijing, the corresponding proportions shifted to 28 % and 22 % (Dada et al., 2020). Vereecken et al. (2017) predicted that in equatorial regions, the contribution of sCIs to the gas-phase conversion of SO_2 to sulfuric acid could reach up to 75 %. Furthermore, simulations using the STOCHEM-CRI global atmospheric chemistry and transport model demonstrated (Khan et al., 2018) that the SO_2 oxidation contribution from sCIs significantly exceeds that of OH radicals in terrestrial rainforests and high-latitude boreal forests. This pronounced variability is primarily driven by two intertwined factors. First, considerable uncertainty in numerical simulations arises from inherent limitations in our understanding of CIs chemical kinetics. With continuous breakthroughs in monitoring technologies, the scientific understanding of CI evolution processes is dynamically evolving, resulting in discrepancies in the reaction rate coefficients incorporated into models across different periods. Notably, the unimolecular decomposition rates of CIs/sCIs and the bimolecular reaction rates of sCIs with water monomers and dimers ($H_2O/(H_2O)_2$) exert a decisive influence on numerical calculations (Sarwar et al., 2014). For example, a modeling study under summer conditions in the eastern United States demonstrated that once the competitive reaction between sCIs and $H_2O/(H_2O)_2$ was introduced, the sCI-driven enhancement in surface sulfate plummeted from 18 % to less than 0.5 % (Li et al., 2013). Similarly, in simulations of nocturnal power plant plumes in the southeastern US, whether CI thermal decomposition was considered led to a seven-fold difference in the estimated contribution to secondary sulfate aerosol (SSA) formation (Meidan et al., 2019). Second, pronounced regional heterogeneity in precursor composition, such as biogenic isoprene and monoterpenes in forested regions and complex anthropogenic alkene mixtures in urban areas, together with differ-

ences in relative humidity and NO_x levels, leads to highly variable sCI production and scavenging fluxes. While existing studies have made progress in quantifying the contribution of sCIs to gas-phase SO_2 oxidation in specific environments and identifying their precursors, the relationship between sCIs and their precursors remains unclear. Consequently, a systematic understanding of the critical driving factors dictating the relative contribution of sCIs is still lacking. Moreover, the production and loss processes of OH and sCIs are not mutually independent; rather, they are deeply coupled within the underlying chemical mechanisms (Lu et al., 2019). This coupled nature dictates that when evaluating the drivers controlling the contribution of the sCIs + SO_2 pathway, their concurrent impacts on the OH + SO_2 pathway and the overall SO_2 oxidation rate cannot be overlooked. Fundamentally, the interplay between precursor abundances and competitive sinks determines the fractional contribution of the sCIs pathway. Yet, how this interplay shapes the sensitivity of the total gas-phase SO_2 oxidation to environmental drivers has received remarkably little attention. In particular, it remains elusive how the dominant controlling factors and their directional impacts shift as the atmospheric gas-phase SO_2oxidation regime transitions from being strictly OH-dominated to being co-driven by both OH and sCIs.

To this end, this study presents a systematic assessment of the role of sCIs in atmospheric SO_2 gas-phase oxidation. As a prerequisite for all subsequent analyses, we first updated the gas-phase kinetics of Criegee intermediates in the Master Chemical Mechanism (MCM v3.3.1, via website: https://mcm.york.ac.uk, last access: 28 August 2026) using the latest evaluated rate coefficients recommended by the International Union of Pure and Applied Chemistry (IUPAC), thereby minimizing the propagation of mechanistic uncertainties into our conclusions. Utilizing an atmospheric box model coupled with this revised mechanism, we integrated interpretable machine learning techniques to quantify the importance of key controlling factors on sCI-mediated SO_2oxidation. Building on this insight, we employed a robust experimental design to construct a machine learning surrogate model capable of predicting sCI contributions across diverse and highly variable environmental conditions. Furthermore, analytical methods, including SHAP, Sobol sensitivity analysis, Partial Dependence Plots (PDPs), and individual conditional expectation (ICE) plots, were utilized to quantify how these factors dictate the relative contribution of sCIs, and to elucidate the differential sensitivities of total SO_2 oxidation under high- and low-sCI contribution regimes. Finally, leveraging online hourly observational data of atmospheric pollutants, we assessed the disparities in their sensitivity relationships with SO_4^{2-} across varying sCI contribution levels, ultimately validating the reliability of our box model-derived surrogate model.

2 Data and methodology

2.1 Updates to alkene ozonolysis and Criegee intermediate chemistry in MCM v3.3.1

The Master Chemical Mechanism (MCM v3.3.1; available at http://mcm.york.ac.uk, last access: 28 August 2026) is a near-explicit chemical mechanism that describes the gas-phase oxidation of 143 volatile organic compounds (VOCs) to carbon dioxide (CO_2) and water (H_2O). In MCM v3.3.1, the rate coefficients and associated reaction mechanisms for alkene ozonolysis reactions follow the recommendations of Jenkin et al. (1997, 2015) and Saunders et al. (2003). Although this mechanism provides a detailed representation of CI formation, loss, and subsequent chemical evolution, several key rate coefficients and parameters differ substantially from the latest IUPAC recommendations (Cox et al., 2020). In addition, several important processes are not explicitly represented, including the specific fates of CIs, the unimolecular decomposition of sCIs, the reactions of sCIs with water dimers ($(H_2O)_2$), and the distinct reactivities of sCI stereoisomers. To address these limitations, we updated the gas-phase alkene + O_3 chemistry in MCM v3.3.1 primarily in accordance with current IUPAC recommendations. The updates include the alkene ozonolysis rate coefficients ($k_{O3+alkene}$), OH yields ($Y_{i,OH}$), sCI yields ($Y_{i,sCI}$), and sCI bimolecular reaction rate coefficients (k_b), as well as accounting for sCI unimolecular decomposition pathways and adding sCI + $(H_2O)_2$ reactions. Where IUPAC provides temperature-dependent kinetic expressions, these were adopted; in addition, a temperature-dependent rate expression was incorporated for the $CH_2OO + SO_2$ reaction, based on Onel et al. (2021). Specifically, the branching ratios for the unimolecular decomposition or isomerization pathways of CIs and sCIs were constrained using reported OH yields and the yields of other relevant products. For sCIs exhibiting stereoisomerism, including CH_3CHOO, C_2H_5CHOO, and the C_4 intermediates formed during isoprene ozonolysis, the Z-stereoisomers were assumed to undergo predominantly rapid unimolecular decomposition under tropospheric conditions, such that their contribution to bimolecular reactions was considered negligible (Newland et al., 2015). Accordingly, in the updated mechanism, hereafter denoted MCM v3.3.1g, stereoisomeric sCIs participating in bimolecular reactions are represented explicitly by their E-stereoisomers. The unimolecular decomposition pathways of sCIs were considered together with the decomposition or isomerization channels of their corresponding chemically activated CIs. The kinetic parameters and product yields for the alkene ozonolysis reactions before and after the updates are summarized in Tables S1 and S2 in the Supplement. The complete set of updated reaction equations, together with the corresponding rate coefficients and explicit branching ratios, is provided in Table S3. These updates were applied to C_1–C_4

Criegee intermediates, which are widely recognized to play a critical role in tropospheric chemistry.

The concentration of $(H_2O)_2$ is determined by assuming rapid thermal equilibrium between water monomers and dimers. Given this fast atmospheric exchange, the dimer concentration is considered to be in thermodynamic equilibrium with the monomer, as expressed in Eq. (1):

$$K_{eq}^{D} = \frac{[(H_2O)_2]}{[H_2O]^2}, \quad (1)$$

where K_{eq}^{D} is the temperature-dependent equilibrium constant for dimer formation (Scribano et al., 2006). Following the methodology of Lade et al. (2024), the reaction of sCIs with water dimers is parameterized using an effective third-order rate coefficient, k_{eff} (cm^6 molec.$^{-2}$ s^{-1}), and the rate of sCI loss via reaction with water dimers, $r_{sCI+(H_2O)_2}$, is given by Eq. (2):

$$\begin{aligned} r_{sCI+(H_2O)_2} &= k_{b,dimer}[sCI]\left[(H_2O)_2\right] \\ &= k_{b,dimer}K_{eq}^{D}[sCI][H_2O]^2 \\ &= k_{eff}[sCI][H_2O]^2, \end{aligned} \quad (2)$$

where k_{eff} is defined as the product of the bimolecular rate coefficient for the sCI + $(H_2O)_2$ reaction ($k_{b,dimer}$, cm^3 molec.$^{-1}$ s^{-1}) and K_{eq}^{D}. To calculate K_{eq}^{D} accurately, thermochemical data were retrieved from the Active Thermochemical Tables (ATcT). Standard Gibbs free energies of formation ($\Delta_f G_T^{\circ}$) for both the water monomer and dimer were extracted from Tables 1 and 3 in Ruscic (2013). These discrete data points were then used to calculate the reaction Gibbs free energy ($\Delta_r G_T^{\circ}$) over the temperature range of 200–360 K, which spans typical tropospheric conditions. The temperature dependence of K_{eq}^{D} was subsequently obtained via a linear regression of $\ln\left(K_{eq}^{D}\right)$ as a function of $\frac{1}{T}$, yielding the following empirical van't Hoff–type parameterization in Eq. (3):

$$K_{eq}^{D}(T) = A\exp\left(\frac{B}{T}\right), \quad (3)$$

where the coefficients A and B represent the intercept and slope, respectively, derived from the fitting procedure, with $A = 1.15 \times 10^{-23}$ cm^3 molec.$^{-1}$ and $B = 1549.32$ K.

2.2 Box model configuration and observation data

2.2.1 AtChem model setup and chemical diagnostics

AtChem (Sommariva et al., 2020), an open-source zero-dimensional atmospheric box model, was used in this study to simulate the gas-phase chemical evolution of SO_2, CIs, and their precursors. The AtChem model is coupled with MCM v3.3.1 and MCM v3.3.1g (see Sect. 2.1). H_2O concentrations for sCI loss reactions were calculated from relative humidity, temperature, and atmospheric pressure.

Two types of AtChem simulations were performed in this study. The first used an unconstrained configuration, in which the initial concentrations of selected chemical species were prescribed and allowed to evolve according to the chemical mechanism without time-varying constraints. This configuration was used in Sect. 3.1 to quantify the oxidation capacity of sCIs derived from the ozonolysis of specific alkenes, including ethene, propene, but-1-ene, *trans*-but-2-ene, *cis*-but-2-ene, 2-methylpropene, and isoprene. The second used a constrained configuration, in which selected trace gases, meteorological parameters, and photolysis frequencies were prescribed as hourly time-varying inputs from observational data or designed perturbation scenarios. This configuration was used in Sect. 3.2 and 3.3 to evaluate the role of sCIs in gas-phase SO_2 oxidation under atmospherically relevant conditions. A spin-up period of 2–3 d was implemented to initialize reactive free radicals and intermediates, such as OH, HO_2, RO_2, and sCIs, allowing them to reach realistic steady-state concentrations.

Chemical production and loss rates were quantified using the Rate of Production/Destruction Analysis (ROPA/RODA) within AtChem. The gas-phase SO_2 oxidation rate by sCIs was defined according to Eq. (4):

$$L_{SO_2,sCIs} = \sum\nolimits_i k_{SO_2+sCI}[sCI_i][SO_2], \quad (4)$$

where i denotes an individual sCI species. The OH-driven SO_2 oxidation rate was defined as in Eq. (5):

$$L_{SO_2,OH} = k_{SO_2+OH}[OH][SO_2], \quad (5)$$

The total gas-phase SO_2 oxidation rate and the fractional sCI contribution were then calculated as in Eqs. (6) and (7):

$$L_{SO_2} = L_{SO_2,sCIs} + L_{SO_2,OH}, \quad (6)$$

$$\mu_{sCIs} = \frac{L_{SO_2,sCIs}}{L_{SO_2}}, \quad (7)$$

here, $L_{SO_2,sCIs}$ and μ_{sCIs} provide complementary perspectives on the absolute rate and fractional contribution, respectively, of the sCI pathway.

2.2.2 Observation data

The observational data used in this study were obtained from the automatic monitoring system at the Wuhai City Atmospheric Environment Super Monitoring Station from 9 October 2019 to 30 June 2022. Wuhai is a semi-arid coal-chemical industrial city in Inner Mongolia, China, characterized by relatively high emissions of SO_2 and anthropogenic VOCs (including alkenes), frequent O_3 pollution, and comparatively dry atmospheric conditions. The dataset includes air pollutants ($PM_{2.5}$, carbon monoxide (CO), SO_2, nitric oxide (NO), nitrogen dioxide (NO_2), and ozone (O_3)), meteorological variables (wind speed (WS), temperature (T),

pressure (P), and relative humidity (RH)), water-soluble inorganic ions (including NO_3^- and SO_4^{2-}), elemental components (including Fe), VOCs, and photolysis frequencies. $PM_{2.5}$, NO, NO_2, SO_2, CO, and O_3 were measured using a Metone BAM-1020 $PM_{2.5}$ Monitor, an API T201 NH_3–NO_x Analyzer, an API T100 SO_2 Analyzer, an API T300 CO Analyzer, and an API T400 O_3 Analyzer, respectively. VOCs were measured using an ENTECH BCT-7800 VOCs Analyzer. Water-soluble inorganic ions were measured using a Metrohm MARGA ADI 2080 online ion chromatograph, and elemental components were measured using a CES Xact-625 atmospheric heavy metal analyzer. Meteorological variables (T, RH, P, WS) were measured using a Lufft WS601-UMB six-parameter meteorological sensor. Photolysis frequencies were measured using a Metcon UF-CCD photolysis spectroradiometer. The observational data had an hourly time resolution and were screened for invalid values. Short missing intervals were linearly interpolated when appropriate, whereas longer gaps were excluded from the analysis.

2.3 Machine learning model and interpretation framework

An interpretable machine learning (ML) framework was developed in this study to systematically evaluate the role of sCIs in SO_2 oxidation, encompassing model development, validation, and interpretation. The learning algorithm used throughout was Extreme Gradient Boosting (XGBoost) (Chen and Guestrin, 2016), which constructs an additive ensemble of regression trees by iteratively minimizing a regularized loss function, with each successive tree fitted to the negative gradients (i.e., pseudo-residuals) of the current ensemble's predictions. This formulation enables nonlinear responses and predictor interactions to be represented far more flexibly than a single regression tree. Regularization, subsampling, cross-validation, and early stopping were applied to suppress overfitting, and hyperparameters were tuned via random search or Bayesian optimization. The same sampling–training–testing workflow was applied to every model in this study. Two classes of XGBoost models were constructed (using the XGBoost Python package, version 2.1.3; https://github.com/dmlc/xgboost, last access: 28 August 2026): surrogate models trained on AtChem-simulated chemical evolution, and an observation-based model trained on ambient measurements. Four complementary interpretation methods were used to explain the XGBoost model outputs: SHAP (SHapley Additive exPlanations), Sobol sensitivity analysis, partial dependence plots (PDPs), and individual conditional expectation (ICE) plots.

2.3.1 Model development details

Three surrogate models were developed based on SO_2 gas-phase oxidation simulations from AtChem to successively quantify the key controls on sCI-mediated SO_2 oxidation, identify the atmospheric conditions under which the sCI pathway becomes important, and examine how this importance affects the sensitivity of total SO_2 oxidation. An observation-based model was developed to assess whether the sensitivities inferred from the surrogate models are also reflected in ambient measurements. These XGBoost models are introduced in turn below.

First, a surrogate model was developed to emulate the sCI-mediated SO_2 oxidation rate ($L_{SO_2,sCIs}$), with SHAP analysis applied to diagnose the contributions of its key controlling factors, namely the principal sCI precursors and competing sinks (most notably NO_2, H_2O, and $(H_2O)_2$). The feature set therefore comprises O_3, RH, NO_2, and six alkene precursors: ethene, propene/but-1-ene, *trans*-but-2-ene, *cis*-but-2-ene, 2-methylpropene, and isoprene, where propene and but-1-ene are merged into a single feature owing to the close similarity of their ozonolysis mechanisms. To capture individual perturbations and interactions across all features, 3898 simulation scenarios were designed spanning the prescribed feature ranges. In each scenario, the feature values prescribed the initial input concentrations for a 1 h unconstrained AtChem simulation, with SO_2 held constant; the mean $L_{SO_2,sCIs}$ over the simulated hour, obtained under both MCM v3.3.1 and v3.3.1g, served as the target output. The resulting feature matrix and corresponding simulation outputs together constitute the training dataset for the surrogate model. The prescribed feature ranges, full scenario design, training details, and model performance are provided in Sect. S1 in the Supplement. Note that in all simulation scenarios, temperature and pressure were held constant at $T = 290$ K and $P = 888$ hPa. Temperature-dependent results for the full scenario set are provided in Sect. S4.

Second, to identify the atmospheric conditions that favor sCI contribution to total gas-phase SO_2 oxidation, a surrogate model was developed to predict the fractional importance of the sCI pathway (μ_{sCIs}), combined with Sobol sensitivity analysis, PDPs, and ICE plots. Unlike $L_{SO_2,sCIs}$, which depends solely on sCI production and loss, μ_{sCIs} is also governed by the parallel OH-mediated oxidation pathway and therefore requires a feature set that captures both sCI and OH chemistry. Accordingly, the feature set comprises O_3, NO_x, NO_2 fraction ($NO_2\,\% = NO_2/NO_x$), total VOC concentration (VOCs), alkene fraction (alkene $\% = \sum$alkenes/VOC), RH, and the Aggregated Reactivity Index (ARI). The NO_x–NO_2 % and VOC–alkene % pairs jointly characterize the oxidant state and reactive VOC composition while minimizing multicollinearity among features. ARI is an ordinal variable encoding the sCI-oxidation potential of the prevailing alkene mixture, derived directly from the importance ranking of alkene features established by the $L_{SO_2,sCIs}$ surrogate model. The training samples generated for this surrogate differ from those of the $L_{SO_2,sCIs}$ model. Rather than prescribing initial concentrations, the feature values here represent normalized scaling factors applied to time-varying constraints, as the AtChem model was run in a constrained con-

figuration. The baseline constraints are the three-year mean diurnal cycles of hourly observations at the Wuhai supersite (Sect. 2.2.2), and the perturbation range of each feature spans the 5th–95th percentile range of the observed concentrations (normalized range is [0, 1]); ARI, as an ordinal discrete variable, is the sole exception and takes integer values of 0, 1, or 2, corresponding to the three tiers of sCI-oxidation potential. Because photolysis frequencies play a decisive role in OH production and radical cycling, daytime and nighttime conditions were treated as entirely separate modeling problems, with target time periods of 08:00–18:00 and 22:00–05:00 LT, respectively. For each scenario, the constraints of the target period were adjusted according to the prescribed feature values, while all remaining constraints (non-feature variables) were held at baseline (Fig. S2 in the Supplement); a constrained AtChem simulation under MCM v3.3.1g then yielded the mean μ_{sCIs} and $L_{\mathrm{SO_2}}$ over the target period as the target outputs. The resulting feature matrix and simulated μ_{sCIs} values together constitute the training datasets for the daytime and nighttime μ_{sCIs} surrogate models. These daytime and nighttime datasets were then each divided into low- and high-μ_{sCIs} subsets based on the median μ_{sCIs} value, and a further pair of surrogate models was developed to predict $L_{\mathrm{SO_2}}$ separately in each regime, combined with partial dependence analysis to assess whether the sensitivity of $L_{\mathrm{SO_2}}$ to each feature depends on the relative importance of the sCI pathway. The baseline constraints, the mapping from normalized feature values to constraint magnitudes, full scenario design, training details, and model performance are provided in Sect. S2.

Finally, to assess whether the regime-dependent sensitivities inferred from the surrogate models are also expressed in the real atmosphere, we developed an observation-based model trained on ambient observations from the Wuhai supersite (9 October 2019 to 30 June 2022, hourly resolution) to predict $\mathrm{SO_4^{2-}}$. The features, including $\mathrm{PM_{2.5}}$, $\mathrm{NO_3^-}$, $\mathrm{SO_2}$, $\mathrm{O_3}$, total VOCs, alkene %, NO_x, $\mathrm{NO_2}$ %, RH, wind speed, and Fe, were selected to represent sulfate aerosol precursor abundance, photochemical oxidation capacity, aerosol loading, secondary inorganic aerosol formation, meteorological conditions, and gas-phase and aqueous-phase oxidation pathways. SHAP analysis was applied to evaluate the differential contributions of key features to $\mathrm{SO_4^{2-}}$ under contrasting μ_{sCIs} regimes, enabling comparison with the regime-dependent sensitivities diagnosed from the AtChem-based surrogate models. Training details and model performance are provided in Sect. S3.

2.3.2 Model interpretation methods

In this study, XGBoost was not used merely as a black-box surrogate for predicting chemical reaction rates or target pollutant concentrations. Instead, it served as a computationally efficient emulator of the box-model simulations, enabling systematic sensitivity analysis and interpretation of the chemical response within the prescribed parameter space. To interpret the trained XGBoost models, we combined SHAP analysis, Sobol sensitivity analysis, partial dependence plots, and individual conditional expectation plots. These four approaches were selected to provide complementary perspectives spanning global versus local attribution, main effects versus interaction effects, and average versus sample-level response behavior. Specifically, SHAP values were used to quantify the relative importance and direction of predictor effects at both individual-sample and aggregate levels, while SHAP interaction values were used to diagnose key two-factor interactions. Sobol sensitivity analysis was used to provide a variance-based decomposition of the model output, separating the independent contribution of each input factor from interaction-driven contributions. PDPs were used to visualize the average nonlinear response of the model output to selected predictors and to identify potential thresholds, whereas ICE plots were used to examine whether these average responses were consistent across individual samples or instead varied among different chemical regimes, revealing heterogeneity that PDPs alone cannot capture. For models trained on controlled numerical experiments, the feature values were prescribed through independent, design-of-experiments-based sampling, and the target outputs were generated by a deterministic, mechanism-based chemical model (AtChem). Because the training data are thus not subject to uncontrolled confounding, and because XGBoost was trained to approximate the fixed relationships embedded in the chemical mechanism, the resulting SHAP, Sobol, PDP, and ICE analyses were interpreted as model-estimated chemical sensitivities that reasonably reflect the causal structure inherent in the chemical mechanism, within the sampled parameter space. For the model trained on ambient observations, by contrast, the input features are inherently correlated, and the observed feature–outcome relationships may be subject to unknown confounding. Consequently, SHAP-based interpretations for this model were treated as statistical associations used to evaluate consistency with the chemical sensitivities inferred from the AtChem-based surrogate models, rather than as evidence of direct causal effects.

1. SHAP (SHapley Additive exPlanations) is a game-theoretic approach for interpreting machine learning model predictions (Lundberg and Lee, 2017; Lundberg et al., 2018). Each input feature is treated as a "player" in a cooperative game, and the model prediction for any individual sample is expressed as an additive decomposition of per-feature contributions. Specifically, for a sample x_i with N features, the predicted value $f(x_i)$ is decomposed as Eq. (8):

$$f(x_i) = \phi_0 + \sum_{j=1}^{N} \phi_j(f, x_i), \tag{8}$$

where $\phi_0 = E\left[f(x)\right]$ is the base value, i.e., the expected model output averaged over the entire dataset,

and $\phi_j(f, x_i)$ is the SHAP value of feature j for sample x_i, quantifying the contribution of feature j to the deviation of the prediction from the base value ϕ_0. The SHAP value $\phi_j(f, x_i)$ is computed as the weighted average marginal contribution of feature j across all possible subsets of the remaining features, as shown in Eq. (9):

$$\phi_j(f, x_i) = \sum_{S \subseteq F \setminus \{j\}} \frac{|S|!(|F| - |S| - 1)!}{|F|!} \left[f(S \cup \{j\}) - f(S) \right], \quad (9)$$

where F is the full set of features, S denotes a subset of features that excludes feature j, and $f(S)$ denotes the conditional expectation of the model output given the features in S. The sign of $\phi_j(f, x_i)$ indicates the direction of the feature effect for a specific sample (positive: the feature j increases the predicted value relative to the baseline; negative: it decreases it), and the magnitude indicates the strength of that effect. For XGBoost models, SHAP values are computed exactly and efficiently using the TreeExplainer algorithm (Lundberg et al., 2020).

The global importance of feature j is summarized by its mean absolute SHAP value (Eq. 10):

$$\overline{|\phi_j|} = \frac{1}{n} \sum_{i=1}^{n} |\phi_j(f, x_i)|, \quad (10)$$

where n is the total number of samples. $\overline{|\phi_j|}$ represents the average magnitude of feature j's contribution to model predictions across the dataset and is used to rank features by their global importance.

Pairwise feature interactions are further quantified via SHAP interaction values (Lundberg et al., 2019). The mean absolute interaction value between features j and p is defined as Eq. (11):

$$\overline{|\phi_{jp}|} = \frac{1}{n} \sum_{i=1}^{n} |\phi_{jp}(f, x_i)|, \quad (11)$$

where $\phi_{jp}(f, x_i)$ is the SHAP interaction value between features j and p for sample x_i, quantifying the portion of their joint effect on the prediction.

2. A variance-based global sensitivity analysis was performed using the Sobol method (Saltelli et al., 2010; Sobol, 2001). Sobol analysis decomposes the variance of the model output into contributions from individual input factors and their interactions over a prescribed input space and probability distribution. It thereby provides a global measure of sensitivity that is not determined by the empirical distribution of the training data.

   For a model output $Y = f(x)$, where x_1, x_2, …, x_N denote N mutually independent input factors, the total output variance, $\mathrm{Var}(Y)$, can be decomposed into contributions from individual factors and their interactions (Eq. 12):

$$\mathrm{Var}(Y) = \sum_{j=1}^{N} V_j + \sum_{j<k} V_{jk} + \ldots, \quad (12)$$

   where $V_j = \mathrm{Var}_{x_j}\left[E_{x_{\sim j}}(Y|x_j)\right]$ is the variance attributable to the main effect of x_j, whereas V_{jk} represents the additional variance attributable to the interaction between x_j and x_k. Higher-order terms represent interactions involving three or more input factors.

   Two Sobol sensitivity indices were computed for each input factor. The first-order index, S_j, quantifies the proportion of output variance attributable to the main effect of x_j (Eq. 13):

$$S_j = \frac{V_j}{\mathrm{Var}(Y)}, \quad (13)$$

   The total-order index, S_{T_j}, quantifies the contribution of x_j to the output variance, including its main effect and all interaction effects involving x_j (Eq. 14):

$$S_{T_j} = \frac{E_{x_{\sim j}}\left[\mathrm{Var}_{x_j}(Y|x_{\sim j})\right]}{\mathrm{Var}(Y)} = 1 - \frac{\mathrm{Var}_{x_{\sim j}}\left[E_{x_j}(Y|x_{\sim j})\right]}{\mathrm{Var}(Y)}, \quad (14)$$

   where $x_{\sim j}$ denotes all input factors except x_j. Under the assumed independent input distributions, both indices range from 0 to 1. The difference, $S_{T_j} - S_j$, quantifies the cumulative contribution of interaction effects involving x_j. Thus, values of S_{T_j} substantially larger than S_j indicate that x_j participates strongly in non-additive interactions with other predictors, an effect that cannot be identified from main-effect rankings alone.

   Input samples for the Sobol sensitivity analysis were generated using the Saltelli sampling scheme based on Sobol' quasi-random sequences (Saltelli, 2002). For each continuous input factor, the sampling bounds were defined by the minimum and maximum values in the training dataset, and samples were generated independently over these bounds. A base sample size of 32 768 was used. Following the Saltelli sampling scheme with second-order effects enabled, this resulted in 524 288 surrogate-model evaluations for the seven input factors. This large evaluation budget was made computationally efficient by the trained XGBoost surrogate model, which evaluates each scenario several orders of magnitude faster than the corresponding box-model simulation. For ARI, which was encoded as an ordinal variable with integer values of 0, 1, and 2, the continuous Saltelli samples generated over [0, 2] were rounded to the nearest integer and clipped to the valid range to match the representation used for model training. Sobol indices, including first-order and total-order indices, were estimated using the SALib library (Herman and Usher, 2017). Bootstrap 95 % confidence intervals were estimated for all Sobol indices.

3. Partial dependence plots (PDPs) were used to visualize the model-predicted average relationship between selected factors and the target variable (Friedman, 2001). For a factor x_p and the complementary factor set x_c, the

one-dimensional partial dependence function is defined in Eq. (15):

$$\hat{f}_p\left(x_p\right) = E_{x_c}\left[f\left(x_p, x_c\right)\right] \approx \frac{1}{n}\sum_{i=1}^{n} f\left(x_p, x_c^{(i)}\right), \quad (15)$$

where the expectation is approximated by averaging the surrogate model predictions ($\hat{f}_p$) over all n training samples, while fixing x_p at each point of a prescribed grid.

Two-dimensional PDPs were further constructed for selected factor pairs to visualize their joint dependence on the target variable. For a factor pair (x_p, x_q), the two-dimensional partial dependence function is defined in Eq. (16):

$$\hat{f}_{pq}\left(x_p, x_q\right) = E_{x_c}\left[f\left(x_p, x_q, x_c\right)\right] \approx \frac{1}{n_{\mathrm{MC}}}\sum_{i=1}^{n_{\mathrm{MC}}} f\left(x_p, x_q, x_c^{(i)}\right), \quad (16)$$

where n_{MC} denotes a Monte Carlo subsample of the training data used to reduce computational cost over the two-dimensional grid.

4. Individual conditional expectation (ICE) plots were used to complement the PDP analysis by examining the model response at the individual-sample level (Goldstein et al., 2015). Whereas a PDP describes the average model-predicted relationship between a factor and the target variable across samples, an ICE plot displays a separate conditional response curve for each sample. For each curve, the factor of interest is varied across a prescribed grid, while all remaining factors are held at their sample-specific values.

3 Results and discussion

3.1 Effects of key controlling factors on sCI-mediated SO_2 oxidation

sCIs are short-lived reactive intermediates generated from the ozonolysis of alkenes. Their contribution to gas-phase SO_2 oxidation is governed jointly by their atmospheric steady-state concentration and their bimolecular rate coefficient with SO_2. The steady-state concentration is itself determined by the initial ozonolysis rate coefficient, the total sCI yield, and the structure-dependent reactivities of individual sCI species toward other competing sinks – most notably H_2O, $(H_2O)_2$, and NO_2 – which collectively regulate the fraction of sCIs available to react with SO_2. We therefore introduce the sCI-mediated SO_2 oxidation rate, $L_{SO_2,sCIs}$, as the target variable, which simultaneously accounts for sCI production and the effective SO_2 oxidation capacity. Figure 1a and b show that, in both MCM v3.3.1 and MCM v3.3.1g, alkene and O_3 concentrations are positively correlated with $L_{SO_2,sCIs}$, whereas RH and NO_x exhibit marked negative correlations. This pattern is consistent with alkenes and O_3 driving sCI production, while $H_2O/(H_2O)_2$ and NO_2 act as competing sinks that reduce the fraction of sCIs available to react with SO_2. Notably, updating the mechanism substantially increases the magnitude of the absolute SHAP (|SHAP|) values across all features (Fig. 1c), with the average |SHAP| value ranging from 211.9 to 11 177.3 molec. cm^{-3} s^{-1} in MCM v3.3.1, versus 694.0 to 30 429.5 molec. cm^{-3} s^{-1} in MCM v3.3.1g. This indicates that the updated mechanism yields a substantially stronger sensitivity of $L_{SO_2,sCIs}$ to perturbations in environmental and precursor variables, such that the same change in a given feature produces a larger response in $L_{SO_2,sCIs}$. Importantly, the update does not amplify the influence of all features to the same degree; rather, it also reshapes the relative importance attributed to individual alkenes (Fig. 1d). In MCM v3.3.1, the alkene relative importance follows the order: *trans*-but-2-ene (TBUT2ENE, 21.5 %) > *cis*-but-2-ene (CBUT2ENE, 17.6 %) > isoprene (C_5H_8, 9.5 %) > 2-methylpropene (MEPROPENE, 4.3 %) > ethene (C_2H_4, 0.7 %) > propene/but-1-ene (C_3C_4, 0.5 %). In MCM v3.3.1g, isoprene becomes the most important alkene feature (23.8 %), followed by *trans*-but-2-ene (11.0 %), *cis*-but-2-ene (9.7 %), and 2-methylpropene (6.0 %), while ethene (0.9 %) and propene/but-1-ene (0.7 %) remain minor contributors. The approximately sixfold increase in the average isoprene |SHAP| value, rising from 3773.1 to 24 500.7 molec. cm^{-3} s^{-1} after the mechanism update, is markedly larger than the corresponding shift observed for any other alkene. Indeed, prior studies have shown that regions with intense biogenic emissions tend to exhibit elevated sCI-mediated SO_2 oxidation rates, an effect attributed primarily to sCIs derived from isoprene (Hata et al., 2023; Kukui et al., 2021). It should be noted, however, that the relative importance ranking obtained here reflects each alkene's attributed contribution when all alkenes are perturbed over an identical concentration range (0.1–20 ppb); by contrast, isoprene's prominence in previous field and modeling studies may partly reflect its typically higher ambient concentration relative to other alkenes, rather than solely an intrinsically higher sCI reactivity. Within the present perturbation ranges (O_3: 2–90 ppb; each alkene: 0.1–20 ppb; RH: 10 %–80 %), RH emerges as the most influential feature overall, exceeding the attributed importance of every alkene (Fig. 1d). This is consistent with prior kinetic evidence that $H_2O/(H_2O)_2$ dominates the bimolecular loss of sCIs, such that most sCIs have limited capacity to survive under high humidity (Cox et al., 2020; Lade et al., 2024).

The changes in mean absolute SHAP interaction values before and after the update (Fig. 2) further clarify the mechanistic origin of the differential amplification magnitudes in alkene attribution. In MCM v3.3.1g, the elevated SHAP interaction values involving RH with both O_3 and

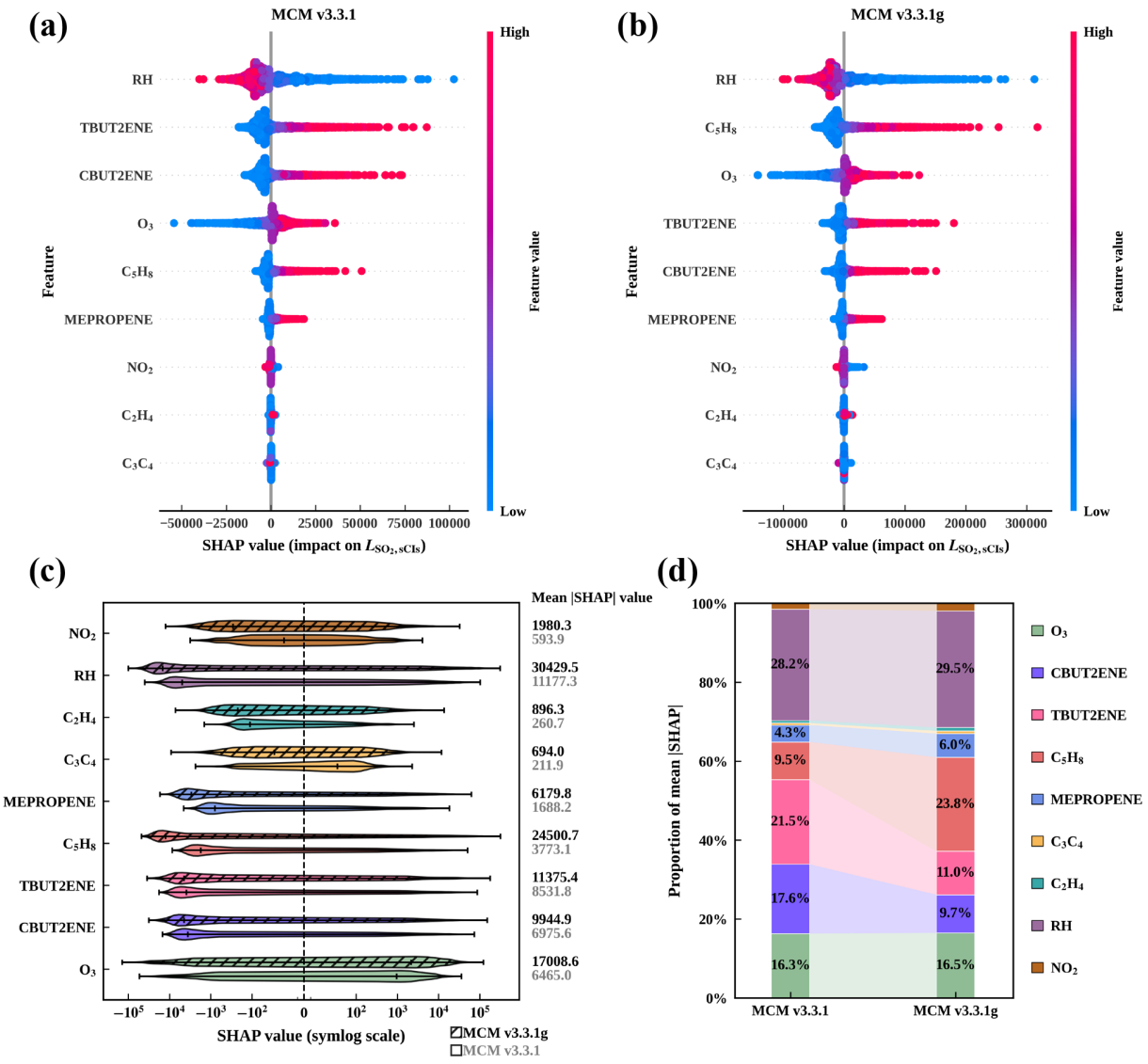

Figure 1. SHAP beeswarm summary plots for the XGBoost surrogate models of $L_{SO_2,sCIs}$ under **(a)** MCM v3.3.1 and **(b)** MCM v3.3.1g. Each point represents one simulation scenario, positioned according to its SHAP value (molec. cm^{-3} s^{-1}) for the corresponding feature. Point color denotes the feature value from low to high. Features are ordered by mean absolute SHAP value, so that those at the top exert the strongest overall influence on the predicted sCI-driven SO_2 oxidation rate. **(c)** Comparison of SHAP-value distributions for individual features between the XGBoost surrogate models trained on MCM v3.3.1 and MCM v3.3.1g. Boxplots summarize the full distribution of SHAP values across all simulation scenarios. Differences between mechanism versions reflect how the kinetic update changes the magnitude of feature effects. **(d)** Relative feature contributions to the XGBoost surrogate models of $L_{SO_2,sCIs}$ under MCM v3.3.1 and MCM v3.3.1g, quantified as the normalized mean absolute SHAP value of each feature. Contributions are expressed as fractions of the total sum of mean absolute SHAP values across all features for each model. This comparison highlights how the mechanism update redistributes the overall importance among ozonolysis precursors and competing sinks.

the individual alkenes indicate that MCM v3.3.1 substantially underestimated the competitive scavenging of sCIs by $H_2O/(H_2O)_2$, thereby masking the strong regulatory role of humidity in sCI-mediated SO_2 oxidation. In parallel, the interaction effects between O_3 and the individual alkenes are also enhanced in MCM v3.3.1g, indicating that MCM v3.3.1 likewise underestimated the sCI + SO_2 oxidation capacity. Critically, the relative degree of underestimation in these two competing removal pathways differs across alkene systems. For isoprene, the RH–C_5H_8 interaction increased from 928.0 to 5094.0 molec. cm^{-3} s^{-1} (a 5.5-fold increase), whereas the O_3–C_5H_8 interaction increased from 697.3 to 4435.3 molec. cm^{-3} s^{-1} (a 6.4-fold increase). This indicates that MCM v3.3.1 underestimated the reactivity of its derived

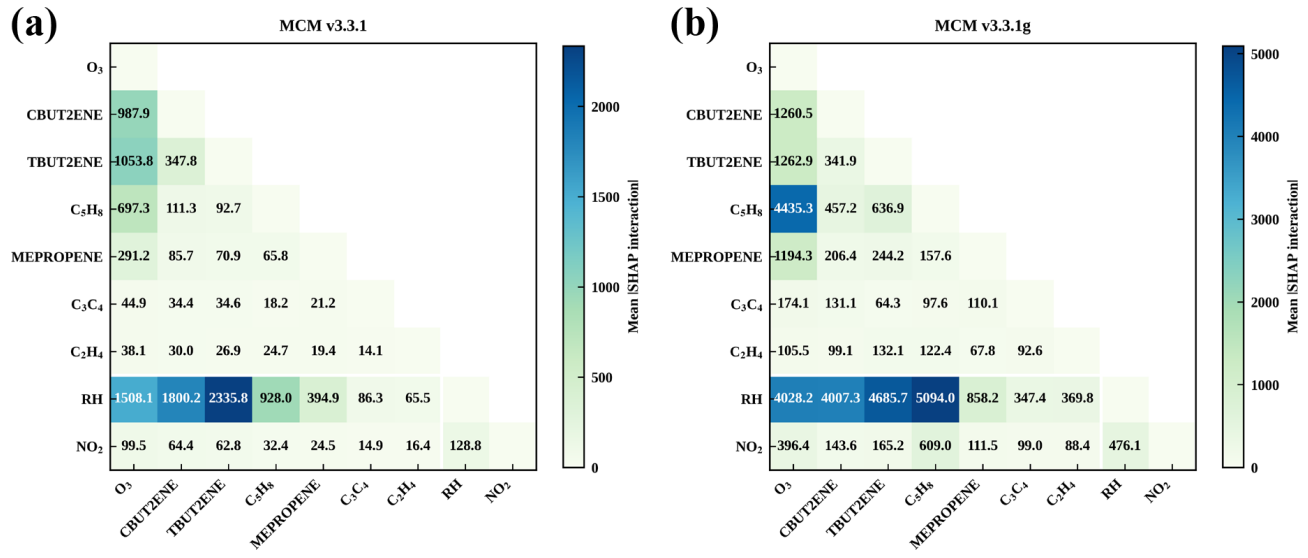

Figure 2. Heat maps of pairwise SHAP interaction values among the nine input features for the XGBoost surrogate models of $L_{SO_2,sCIs}$ under **(a)** MCM v3.3.1 and **(b)** MCM v3.3.1g. Colours denote the mean absolute SHAP interaction value for each feature pair across all simulation scenarios. Larger values indicate stronger non-additive interactions in the surrogate prediction, thereby highlighting the precursor–sink combinations that most strongly modulate sCI-driven SO_2 oxidation.

sCIs toward SO_2 to a greater extent than their reactivity toward $H_2O/(H_2O)_2$; a comparable pattern is observed for 2-methylpropene. For the remaining alkenes, by contrast, the underestimation of the sCI+$H_2O/(H_2O)_2$ pathway predominates.

Based on the MCM v3.3.1g results, isoprene contributes more than twice as much as *cis*-/*trans*-but-2-ene, 3.8 times as much as 2-methylpropene, and roughly thirty times more than ethene and propene/but-1-ene in terms of their attributed influence on $L_{SO_2,sCIs}$ (Fig. 1c). At 298.15 K, the ozonolysis rate coefficients span more than two orders of magnitude (Table S1), following the order: *trans*-but-2-ene (2.0×10^{-16} cm^3 molec.$^{-1}$ s^{-1}) > *cis*-but-2-ene (1.3×10^{-16} cm^3 molec.$^{-1}$ s^{-1}) > isoprene (1.28×10^{-17} cm^3 molec.$^{-1}$ s^{-1}) ≈ 2-methylpropene (1.15×10^{-17} cm^3 molec.$^{-1}$ s^{-1}) ≈ propene (1.05×10^{-17} cm^3 molec.$^{-1}$ s^{-1}) ≈ but-1-ene (1.00×10^{-17} cm^3 molec.$^{-1}$ s^{-1}) > ethene (1.56×10^{-18} cm^3 molec.$^{-1}$ s^{-1}). Total sCI yields follow the sequence (Tables S1 and S3): isoprene (0.66; 0.55 CH_2OO +0.08 $(CH{=}CH_2)(CH_3)COO$ +0.03 $(C(CH_3){=}CH_2)CHOO$) > ethene (0.42; CH_2OO) > propene (0.28; 0.20 CH_2OO +0.08 CH_3CHOO) > but-1-ene (0.23; 0.15 CH_2OO +0.08 C_2H_5CHOO) ≈ *trans*-but-2-ene (0.22; CH_3CHOO) ≈ *cis*-but-2-ene (0.20; CH_3CHOO) ≈ 2-methylpropene (0.20; 0.13 CH_2OO +0.07 $(CH_3)_2COO$). Beyond overall yield, sCI speciation varies considerably: aside from *cis*- and *trans*-but-2-ene, CH_2OO is the dominant sCI across all remaining alkene systems. Critically, the bimolecular reactivities of sCIs are strongly structure-dependent. With respect to SO_2 oxidation, CH_3CHOO, C_2H_5CHOO, $(CH_3)_2COO$, and $(C(CH_3){=}CH_2)CHOO$ exhibit rate coefficients three to four times higher than those of CH_2OO and $(CH{=}CH_2)(CH_3)COO$. The reactivity order toward $H_2O/(H_2O)_2$ is markedly different, however, broadly following $CH_3CHOO \approx C_2H_5CHOO > CH_2OO > (CH{=}CH_2)(CH_3)COO \approx (CH_3)_2COO \gg (C(CH_3){=}CH_2)CHOO$. These contrasts in sCI fate, including ozonolysis kinetics, effective sCI yield (i.e., the fraction of sCIs that persist to undergo bimolecular reactions), and the relative importance of sCI+SO_2 vs. sCI+$H_2O/(H_2O)_2$ pathways, collectively shape the relationship between alkenes and $L_{SO_2,sCIs}$. Hence, the capacity of different alkene ozonolysis systems to oxidize SO_2 cannot be reduced to ozonolysis kinetics and sCI yield alone; the competitive removal of sCIs by $H_2O/(H_2O)_2$ should also be considered (Fig. 2b). A previous H_2SO_4 proxy study similarly noted that the apparent rate constant describing the alkene ozonolysis source spans nearly three orders of magnitude in the real atmosphere, reflecting the underlying complexity of sCI chemistry (Yang et al., 2021).

Figure3 further shows the effects of various alkenes on $L_{SO_2,sCIs}$ at different RH under MCM v3.3.1g, illustrating the regulatory role of the sCI+$H_2O/(H_2O)_2$ pathway. Consistent with the average |SHAP| ranking, isoprene, *trans*-but-2-ene, *cis*-but-2-ene, and 2-methylpropene all exhibit substantially positive impacts of varying degrees as their concentrations increase, whereas ethene and propene/but-1-ene display near-zero or weakly positive dependence across the investigated concentration range. The substantial vertical dispersion at fixed alkene concentrations, observed for all alkenes, indicates that identical alkene abundances can yield markedly

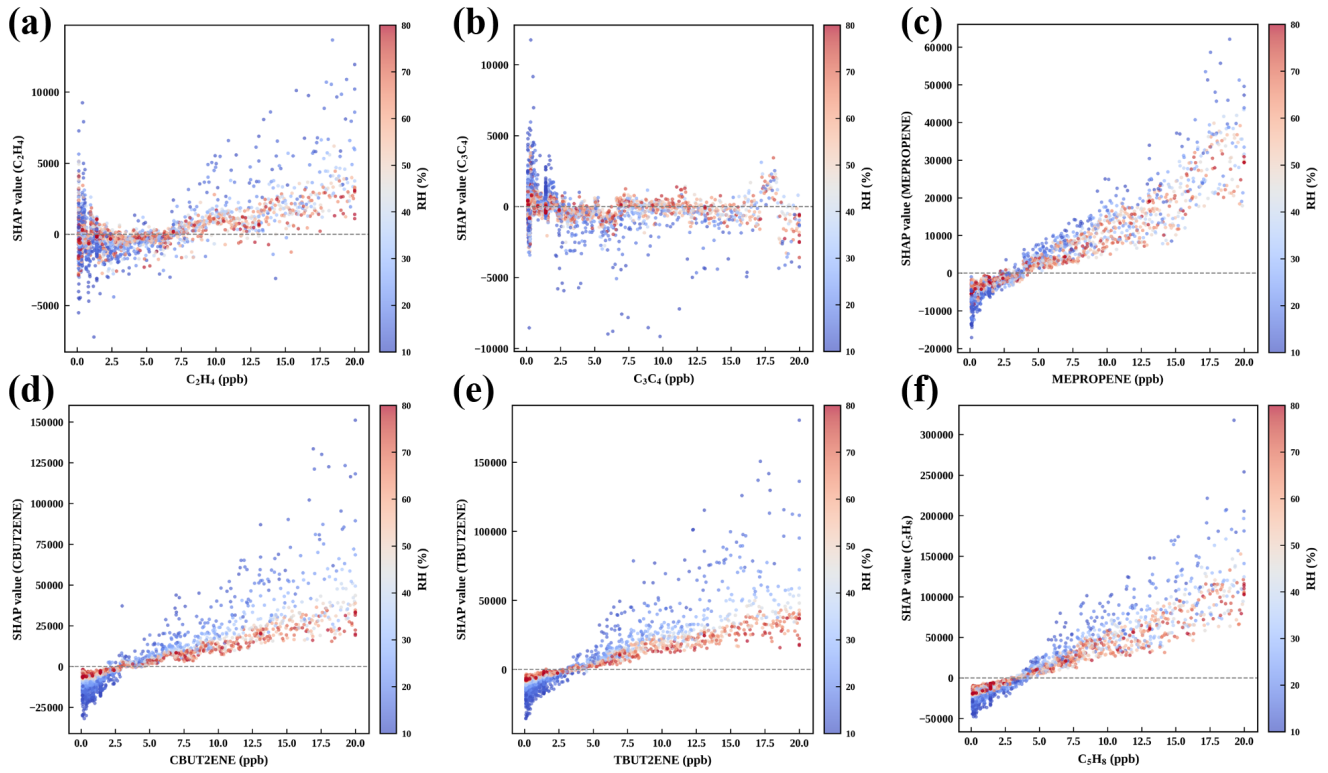

Figure 3. SHAP dependence plots for O_3 and the six alkene precursors – ethene **(a)**, propene/but-1-ene **(b)**, 2-methylpropene **(c)**, *cis*-but-2-ene **(d)**, *trans*-but-2-ene **(e)**, and isoprene **(f)** – in the XGBoost surrogate models of $L_{SO_2,sCIs}$. The *x*-axis shows the feature value, the y-axis shows the SHAP value of the same feature, and point color represents RH. Each point corresponds to one simulation scenario. These plots illustrate the marginal effect of each alkene precursor on the predicted sCI-driven SO_2 oxidation rate and how this effect varies with humidity.

different impacts on $L_{SO_2,sCIs}$, signifying the non-linear responses arising from interaction effects. For most alkenes (excluding propene/but-1-ene), this vertical spread increases with concentration, indicating that higher alkene concentrations expand the range of possible $L_{SO_2,sCIs}$ values, while the realized magnitude remains strongly contingent on ambient conditions. Propene/but-1-ene, by contrast, shows large vertical dispersion across the full concentration range without a significant concentration dependence, suggesting that variability in its SHAP values is driven almost entirely by interaction effects. Ethene similarly shows a significant degree of dispersion in its SHAP values at low concentrations. Taken together, the relationship between alkene concentration and $L_{SO_2,sCIs}$ is nonlinear for all alkenes; however, the degree of nonlinearity differs among alkenes, reflecting differences in the relative strength of their interactions with other feature variables.

We use RH coloring in Fig. 3 to visualize the strength of humidity's interactive effects. Across all alkenes, higher RH consistently suppresses the contributions of alkenes to $L_{SO_2,sCIs}$. The degree of suppression, however, varies markedly with alkene identity, and can be rationalized directly from the kinetic properties of their produced sCIs. Under high-humidity conditions, the contribution of propene/but-1-ene to the variation of $L_{SO_2,sCIs}$ is weak. This is attributable to the relatively low rate coefficients for the reactions of propene/but-1-ene with O_3, which result in significantly lower sCI production than that from ethene and isoprene. The primary sCIs generated from propene/but-1-ene ozonolysis are CH_2OO, CH_3CHOO, and C_2H_5CHOO, all of which react rapidly with $H_2O/(H_2O)_2$. Additionally, CH_2OO, which constitutes the largest proportion, has relatively low reactivity toward SO_2. Consequently, the limited sCIs produced from these two alkenes make a further restricted contribution to sCI-mediated SO_2 oxidation. Ethene, despite having the slowest ozonolysis rate coefficient, produces CH_2OO with a substantially higher yield (0.42) than propene or but-1-ene, partially compensating for its sluggish kinetics. However, since CH_2OO is efficiently scavenged by $H_2O/(H_2O)_2$, ethene's contribution remains small and sensitive to humidity, consistent with the mixed positive and negative SHAP values observed at low concentrations in Fig. 3a. In contrast, *cis*-but-2-ene and *trans*-but-2-ene benefit from both the highest ozonolysis rate coefficients among the investigated alkenes and the exclusive production of CH_3CHOO, which reacts rapidly with SO_2. These

advantages translate into strong positive contributions to $L_{SO_2,sCIs}$; however, because CH_3CHOO is also highly reactive toward $H_2O/(H_2O)_2$, the realized contribution is strongly RH-dependent, as evidenced by the pronounced RH stratification in the dependence plots. 2-methylpropene generates both CH_2OO and $(CH_3)_2COO$. $(CH_3)_2COO$ reacts rapidly with SO_2 but comparatively slowly toward $H_2O/(H_2O)_2$, resulting in weak competition from $H_2O/(H_2O)_2$. This explains why 2-methylpropene shows the smallest vertical dispersion growth with concentration among the more influential alkenes, and why its relationship with $L_{SO_2,sCIs}$ is more nearly linear, since $(CH_3)_2COO$ maintains its reactivity toward SO_2 even under elevated humidity. Isoprene exhibits the strongest positive contribution to $L_{SO_2,sCIs}$ across the full humidity range, arising from the favorable combination of relatively fast ozonolysis, the highest total sCI yield (0.66), and a diverse sCI speciation that includes not only CH_2OO but also $(CH{=}CH_2)(CH_3)COO$ and $(C(CH_3){=}CH_2)CHOO$. $(C(CH_3){=}CH_2)CHOO$ reacts rapidly with SO_2 while undergoing only slow scavenging by $H_2O/(H_2O)_2$, sustaining efficient SO_2 oxidation even at high RH. The interaction between isoprene and RH is thus primarily attributable to the CH_2OO fraction, whereas $(CH{=}CH_2)(CH_3)COO$ and $(C(CH_3){=}CH_2)CHOO$ enable isoprene to remain a dominant driver of $L_{SO_2,sCIs}$ across a wider humidity range. Taken together, when the investigated alkenes are perturbed over the same concentration ranges, ethene and propene/but-1-ene exert negligible direct control on $L_{SO_2,sCIs}$ relative to the remaining alkenes. Isoprene and the C_4 alkenes, *cis-/trans*-but-2-ene and 2-methylpropene, represent the dominant alkene precursors, but their effective impacts are jointly shaped by RH. This finding underscores the need for surrogate modeling to resolve these complex, nonlinear atmospheric reactions into a clear relationship between precursors and $L_{SO_2,sCIs}$. Such modeling enables the identification of key alkene precursors, quantification of the dependence of their contributions on ambient environmental conditions, and elucidation of the key reactions governing their roles in sCI-mediated SO_2 oxidation.

3.2 Controls on the sCIs fractional contribution and regime-dependent sensitivities of SO_2 oxidation

The surrogate model developed in Sect. 3.1 quantifies how key factors govern $L_{SO_2,sCIs}$, the absolute rate of SO_2 oxidation by sCIs. A large $L_{SO_2,sCIs}$, however, does not necessarily imply that sCIs are important for SO_2 oxidation, because their importance also depends on the strength of the parallel OH-driven oxidation pathway. OH and sCIs share certain precursors, but their formation pathways are not entirely identical: alkene ozonolysis simultaneously produces both, so alkenes and O_3 drive both pathways, yet OH is additionally sustained through routes that do not involve sCIs, including RO_x–NO_x radical cycling and the direct photolysis of O_3, HONO, and other species. OH is therefore governed by a broader set of factors, including NO_x, NO_2 %, and the wider VOC composition, several of which exert little or no direct influence on sCI chemistry. As a result, the two oxidation pathways do not respond in tandem to environmental perturbations. Variations in the relative importance of sCIs therefore shape the sensitivity of L_{SO_2} to its controlling factors. To systematically diagnose the atmospheric conditions under which sCIs play a significant role in SO_2 oxidation, and to elucidate how this role modulates the precursor sensitivity of L_{SO_2}, we constructed dedicated surrogate models for μ_{sCIs} and L_{SO_2}. Their feature sets capture the key controls on both pathways (see Sect. 2.3), and the models were trained on a large ensemble of constrained AtChem simulations spanning atmospheric conditions representative of anthropogenically and biogenically influenced environments. Because photolysis exerts decisive control over OH production, daytime (08:00–18:00 LT) and nighttime (22:00–05:00 LT) conditions were analyzed separately.

Sobol sensitivity analysis was applied to identify the dominant atmospheric controls on μ_{sCIs} and to quantify the extent to which each feature exerts its influence independently or through interaction with other features during the daytime period (Fig. 4a). Here, the first-order index S_1 measures the independent main-effect contribution of a single feature, whereas the total-order index S_T additionally encompasses all higher-order interactions involving that feature; a markedly larger S_T relative to S_1 therefore indicates that a feature operates predominantly through coupling with other features rather than through its own variation alone. The analysis identifies ARI, O_3, alkene %, and VOCs as the dominant controls on μ_{sCIs}, with independent contributions ranked as ARI ($S_1 = 0.17$) > alkene % ($S_1 = 0.16$) > O_3 ($S_1 = 0.15$) > VOCs ($S_1 = 0.13$). RH ranks immediately behind ($S_1 = 0.09$), while NO_x and NO_2 % register the weakest direct contributions ($S_1 = 0.03$ and 0.04, respectively). The low-ARI tier (ARI = 0) is dominated by ethene and propene, representative of typical urban anthropogenic emissions (Zhao et al., 2020); the mid-ARI tier (ARI = 1) features an elevated proportion of but-2-ene, characteristic of industrial source environments or marine ecosystems (Giorio et al., 2022); and the high-ARI tier (ARI = 2) is driven primarily by isoprene, representative of biogenic (Rhew et al., 2017) or petrochemical-influenced conditions (Guo et al., 2022). The alkene mixture proportions at each ARI level are detailed in Fig. S1. Comparing S_1 and S_T across all features reveals a clear differentiation in how each feature exerts its influence. For RH, $S_T \approx S_1$ ($S_T = 0.11$), indicating negligible interaction effects; RH influences μ_{sCIs} almost entirely through its independent main effect. For ARI ($S_T = 0.27$), alkene % ($S_T = 0.26$), O_3($S_T = 0.22$), and VOCs ($S_T = 0.23$), S_T substantially exceeds S_1, indicating that although their independent main effects dominate, non-negligible interaction effects are also present. Among these, ARI exhibits both the largest S_1 and S_T, reinforcing that alkene speciation not only exerts the strongest independent control on μ_{sCIs} but also acts

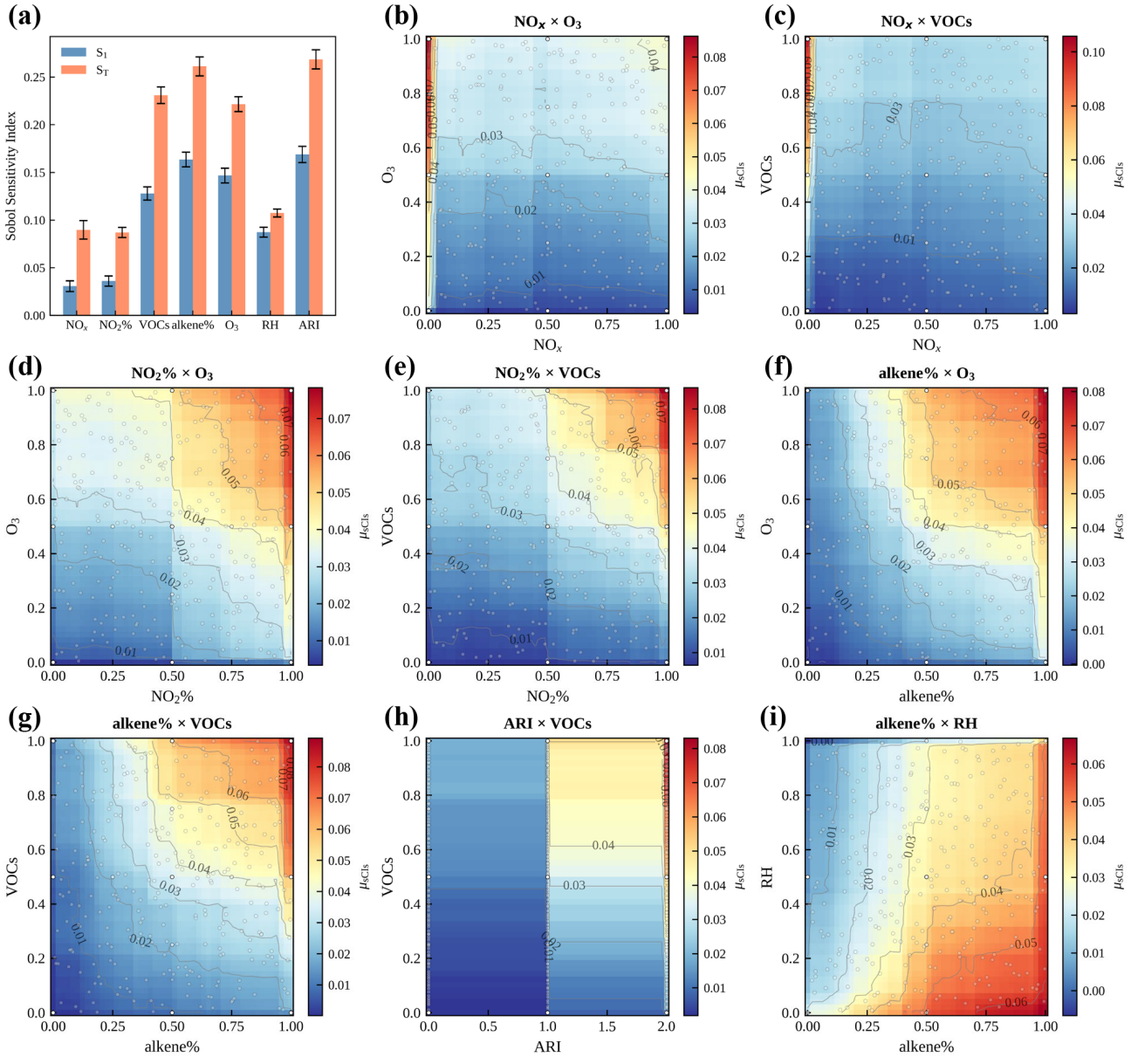

Figure 4. **(a)** First-order (S_1) and total-order (S_T) Sobol sensitivity indices for the seven input features in the XGBoost surrogate model of μ_{sCIs} during daytime. S_1 quantifies the main effect of each feature acting alone, whereas S_T includes both the main effect and all interaction effects involving that feature. The difference between S_T and S_1 therefore reflects the extent to which a feature participates in non-additive interactions. **(b–i)** Two-dimensional partial dependence plots showing the joint effect of O_3norm×NO_xnorm, VOCsnorm×NO_xnorm, O_3norm×NO_2 %norm, VOCsnorm×NO_2 %norm, O_3norm×alkene %norm, VOCsnorm×alkene %norm, VOCsnorm×ARIcode, and RHnorm×alkene %norm on the surrogate-model prediction of μ_{sCIs} during daytime. The surface represents the average model response after marginalizing over the remaining features. Warmer colors indicate larger predicted μ_{sCIs}.

as a key moderator of the effects of O_3, alkene %, and VOCs. The contrast is most pronounced for NO_x and NO_2 %: their S_1 values account for less than half of their respective S_T values (NO_x: $S_T = 0.09$; NO_2 %: $S_T = 0.09$), indicating that their influence on μ_{sCIs} is overwhelmingly mediated through interactions with other features rather than through direct action. This strong interaction dependence reflects the fact that the influence of NO_x and NO_2 % on μ_{sCIs} is conditional on the values of other features.

The directional effects of these features are further illustrated by the 2D PDPs (Fig. 4b–i). Hereafter, feature levels denote normalized values rather than the actual concentrations; corresponding time-varying concentrations are shown in Fig. S1. Among the features that directly govern $L_{SO_2,sCIs}$,

ARI, O_3, VOCs, and alkene % exhibit mutually reinforcing positive effects on μ_{sCIs}, suggesting that conditions favorable for alkene ozonolysis simultaneously enhance the relative competitiveness of the sCI pathway. RH negatively affects μ_{sCIs} by suppressing the sCI+SO_2 pathway through enhanced sCI loss to $H_2O/(H_2O)_2$. Despite NO_2 being a known sCI scavenger, NO_2 % exhibits a synergistic co-enhancement with O_3 and VOCs on μ_{sCIs}. These synergistic effects are expected to arise from the influence of NO_2 % on OH, through its role in governing how NO_x is partitioned between radical termination and cycling (Sillman and He, 2002). A higher NO_2 fraction, at fixed total NO_x, is expected to reduce the NO available for $HO_2/RO_2 \rightarrow$OH conversion, thereby suppressing the SO_2+OH oxidation channel more strongly than it scavenges sCIs, particularly under high-O_3 and high-VOCs conditions. Correspondingly, the higher the NO_2 %, the more strongly μ_{sCIs} increase with rising O_3 and VOCs. NO_x, by contrast, exerts predominantly suppressive interactions with O_3 and VOCs: μ_{sCIs} peaks at the lowest NO_x levels and declines sharply as NO_x increases only slightly from its minimum, before leveling off or increasing slightly at higher concentrations, such that μ_{sCIs} at the highest NO_x level remains well below the peak observed at the lowest NO_x level. The sensitivity of μ_{sCIs} to O_3 and VOCs is modulated by NO_x levels. At the lowest NO_xlevel, increases in O_3 and VOCs produce the largest increments in μ_{sCIs}. Across the remainder of the NO_x range, raising O_3 or VOCs from their minimum to maximum levels increases μ_{sCIs} by only 0.03–0.04. The effect of NO_x on μ_{sCIs} arises primarily from its control over the steady-state OH concentration: at extremely low NO_x level, radical recycling efficiency is greatly diminished, leading to suppressed OH; at excessively high NO_x levels, OH is likewise suppressed, but through accelerated termination reactions between radicals and NO_x. Under both conditions, the attenuation of OH-mediated SO_2 oxidation shifts a greater share of the total oxidation burden to sCIs, resulting in elevated μ_{sCIs}.

Taken together, daytime μ_{sCIs} tends to be elevated under atmospheric conditions characterized by high O_3 concentrations, abundant VOCs, a large alkene fraction, and relatively low RH. With respect to NO_x, μ_{sCIs} is only appreciably enhanced under extremely low NO_x levels; across the remainder of the NO_x range, its influence on μ_{sCIs} is comparatively weak. This finding is consistent with previous studies reporting that sCI chemistry plays a more prominent role in SO_2 oxidation in biogenic-rich forested and rural environments (Kim et al., 2015) than in polluted urban settings (Dada et al., 2020). Among the identified controls, O_3, VOCs, alkene %, and ARI, which collectively characterize conditions favorable for sCI formation, not only directly promote $L_{SO_2,sCIs}$ but also exhibit pronounced synergistic positive effects on μ_{sCIs}. This pattern implies that, as these variables increase, OH increases less strongly than sCI production and may even decrease modestly. Consequently, although O_3 and alkenes jointly initiate the chemical processes leading to the formation of both OH and sCIs, their effects on the OH-mediated and sCI-mediated SO_2 oxidation pathways differ in both magnitude and direction. Under most daytime conditions, the OH pathway dominates SO_2 oxidation, such that the sensitivity of L_{SO_2} to precursor species is primarily shaped by how those precursors affect OH. However, as shown by the NO_x dependence of μ_{sCIs}, the response of OH to precursor perturbations is itself condition-dependent, exhibiting a non-monotonic relationship with NO_x. This gives rise to distinct OH response patterns under high- and low-μ_{sCIs} conditions and, by extension, distinct sensitivities of L_{SO_2} to its precursors. To quantify the magnitude of these differences, the dataset was partitioned into high- and low-μ_{sCIs} subsets based on the median daytime μ_{sCIs} value (1.1 %), and the relationship between each feature and L_{SO_2} was characterized separately for each subset.

Figure 5 illustrates how total gas-phase SO_2 oxidation rate varies with O_3, VOCs, and alkene % across the high- and low-μ_{sCIs} regimes. The mean ICE curves show that L_{SO_2} increases monotonically with all three features under both regimes; however, the response is systematically amplified under high-μ_{sCIs} conditions, with the mean curve exhibiting a steeper and more sustained increase across the full feature range. Beyond the mean response, the spread of individual ICE curves provides insight into response heterogeneity, namely, the extent to which the effect of a given feature on L_{SO_2} varies across different atmospheric conditions. Notably, negative L_{SO_2} responses to increases in VOCs and alkene % are observed under extremely low NO_x level. To quantify this directional heterogeneity, we computed the fraction of individual ICE curves exhibiting a net negative slope between the minimum and maximum feature values, termed the "neg-slope fraction". For O_3, positive associations with L_{SO_2} are nearly universal in both regimes, with a neg-slope fraction of 0 % under the high-μ_{sCIs} regime and 9 % under the low-μ_{sCIs} regime. For alkene %, the neg-slope fraction increases from 7 % under the high-μ_{sCIs} regime to 21 % under the low-μ_{sCIs} regime. A similar pattern is evident for VOCs, with the neg-slope fraction rising from 21 % under high-μ_{sCIs} to 35 % under low-μ_{sCIs} regimes. This regime contrast warrants further examination. At an extremely low NO_x level, high μ_{sCIs} is associated with abundant alkene concentrations. Although higher alkene concentrations may promote radical termination and thereby suppress OH and reduce L_{SO_2}, the high-μ_{sCIs} subset nevertheless exhibits a smaller neg-slope fraction than the low-μ_{sCIs} subset. This suggests that the alkene ozonolysis pathway offsets part of the OH suppression caused by enhanced radical termination, thereby dampening the negative L_{SO_2} response. At moderate-to-high NO_x levels, positive L_{SO_2} responses to increases in VOCs, alkene %, and O_3 dominate and are considerably stronger under the high-μ_{sCIs} regime than under the low-μ_{sCIs} regime. This amplified sensitivity likely reflects the fact that high-μ_{sCIs} regime is associated with abun-

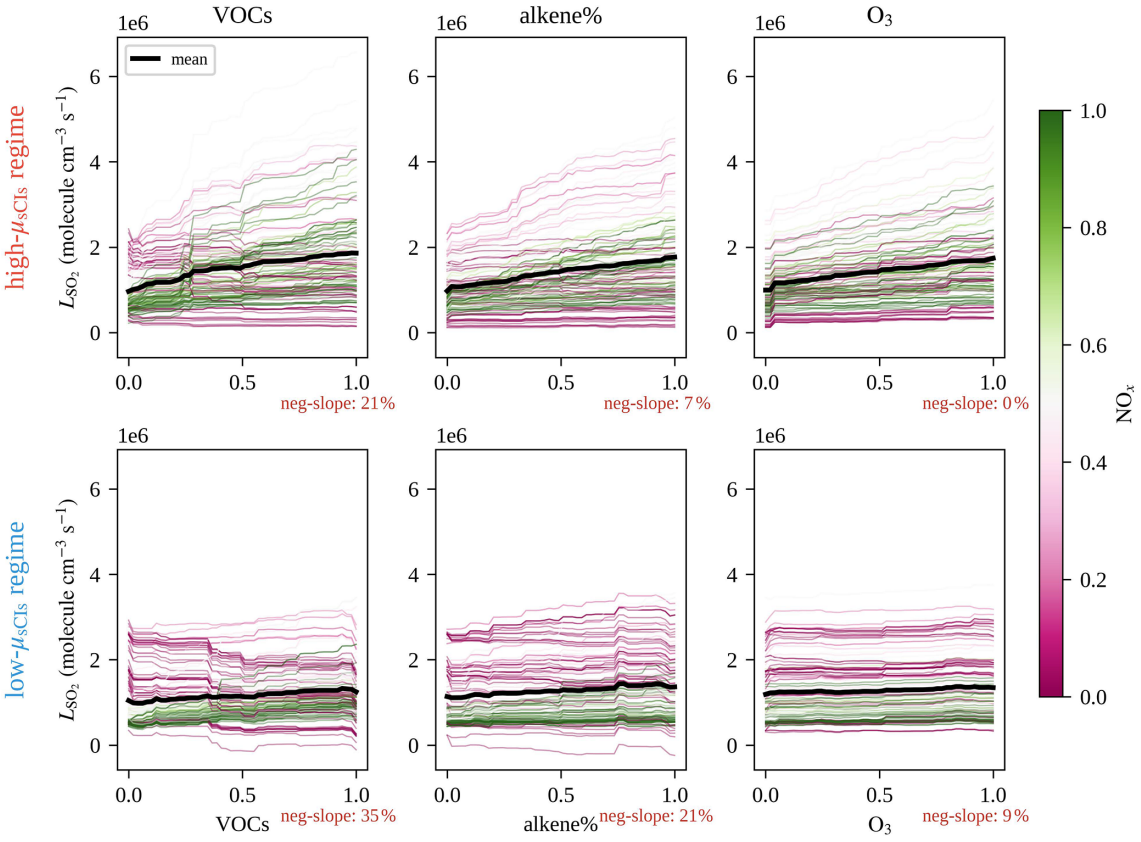

Figure 5. Individual conditional expectation (ICE) plots for the regime-specific L_{SO_2} models during daytime, showing the responses of predicted total gas-phase SO_2 oxidation to VOCsnorm, alkene %norm, and O_3norm in the low- and high-μ_{sCIs} regimes. The two rows correspond to the two μ_{sCIs} regimes, and the three columns correspond to the three selected predictors. Each thin curve represents one sampled scenario, colored by normalized NO_x. The curves are displayed in absolute prediction space (i.e. without centering), so both the slope and vertical spread reflect heterogeneity in the conditional model responses across different chemical backgrounds.

dant alkenes, which simultaneously promote OH propagation through RO_x cycling pathway and drive alkene ozonolysis.

In summary, L_{SO_2} exhibits both positive and negative responses to VOCs and alkene % across the full scenario space, with the key distinction being that under the high-μ_{sCIs} regime, negative responses are less frequent and positive responses are stronger. To clarify the mechanistic basis of this contrast, we examined the OH and sCI budgets for two representative scenarios at normalized NO_x levels of 0 and 0.5 (Fig. 6a, b). This analysis was used to explain why negative L_{SO_2} responses to increases in VOCs and alkene % are more frequent in the low-μ_{sCIs} regime. OH production is partitioned into initiation ($\sum OH_{new}$), which encompasses all primary OH production via photolysis and alkene ozonolysis (Sheehy et al., 2010), and propagation (OH_{propag}), defined as the rate of $HO_2 \rightarrow OH$ conversion. At an extremely low NO_x level (NO_x, norm = 0), the ozonolysis pathway accounts for 39.65 % of $\sum OH_{new}$ (see Sect. S5 for detailed calculations), and the ratio $OH_{propag}/\sum OH_{new}$ is 3.67, indicating that radical propagation contributes approximately 3.7 times as much OH as primary initiation. At a moderate NO_x level (NO_x, norm = 0.5), the ozonolysis share of $\sum OH_{new}$ decreases to 29.28 %, whereas the $OH_{propag}/\sum OH_{new}$ ratio rises to 6.96, reflecting substantially enhanced radical cycling efficiency, as evidenced by the $HO_2 \rightarrow OH$ conversion rate reaching 7.04×10^8 molec. cm^{-3} s^{-1}. At an extremely low NO_x level, the RO_x recycling is severely suppressed, thus primary OH initiation contributes a correspondingly larger fraction to the total OH budget, and the ozonolysis pathway in turn accounts for a larger share of OH production. Under this condition, the contribution of alkene ozonolysis to OH production can partly offset the suppressive effect of enhanced radical termination on OH, which explains why the neg-slope fraction for L_{SO_2} is smaller in the high-μ_{sCIs} subset than in the low-μ_{sCIs} subset. At a moderate NO_x level, OH is sustained predominantly through radical cycling rather than through photolysis or ozonolysis, and the increase in NO_x additionally enhances HONO photolysis, further diminishing the relative contribution of ozonolysis to OH generation. Under these conditions, perturbations in VOCs and alkene % influence L_{SO_2} primarily through their modulation of OH propagation. Because high-μ_{sCIs} conditions at this NO_x level are associated with

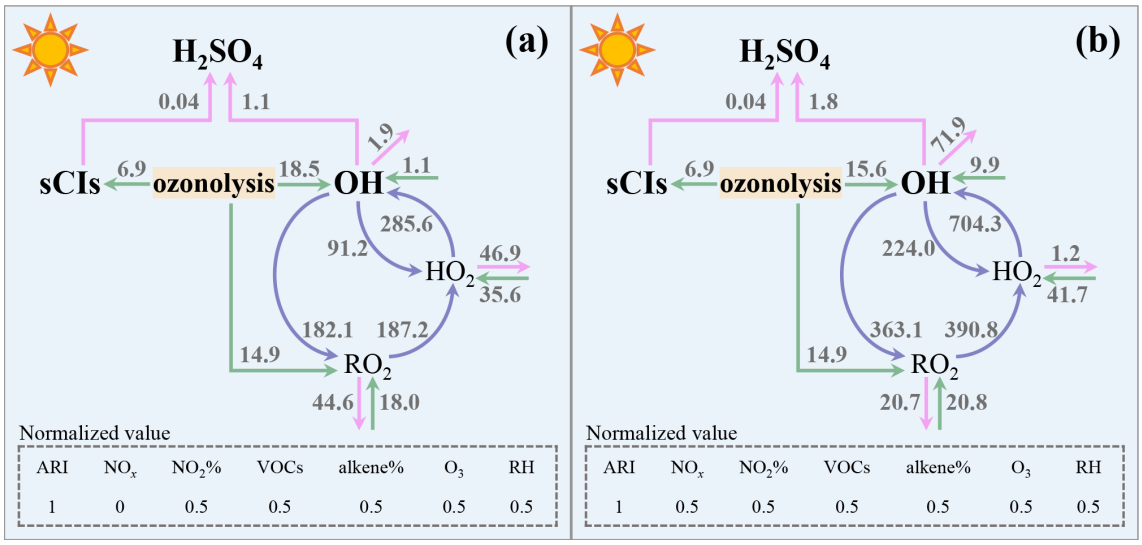

Figure 6. Two representative daytime scenarios illustrating the budgets of OH and sCIs at normalized NO_x levels of **(a)** 0 and **(b)** 0.5. Numbers denote reaction rates (10^6 molec. cm^{-3} s^{-1}). Pink, green, and purple lines indicate the termination, initiation, and propagation pathways of OH and sCIs, respectively.

abundant alkenes, both the RO_x cycling and ozonolysis pathways are strongly activated, and L_{SO_2} therefore exhibits a pronounced positive response to increases in precursor concentrations.

The nighttime Sobol sensitivity indices (Fig. 7a) reveal controls on μ_{sCIs} that differ markedly from those identified during the day. ARI, RH, and NO_x emerge as the dominant controls, with independent contributions ranked as ARI ($S_1 = 0.21$) > RH ($S_1 = 0.19$) > NO_x ($S_1 = 0.17$). VOCs ($S_1 = 0.13$), alkene % ($S_1 = 0.11$), and O_3 ($S_1 = 0.08$) rank immediately behind, while NO_2 % exerts a negligible direct influence ($S_1 = 0.002$). Comparing S_1 and S_T across all features, S_T only slightly exceeds S_1 for most features, indicating that independent main effects dominate and interaction effects are limited, with the total-order ranking following ARI ($S_T = 0.25$) > RH ($S_T = 0.22$) > NO_x ($S_T = 0.20$) > VOCs ($S_T = 0.17$) > alkene % ($S_T = 0.14$) > O_3 ($S_T = 0.10$). NO_2 % retains the smallest S_T ($S_T = 0.02$), reinforcing that its regulatory effect on μ_{sCIs} at night is negligible. The close agreement between S_T and S_1 across most features at night stands in sharp contrast to the daytime results, where S_T substantially exceeded S_1 for several key features. This collapse of interaction effects reflects a fundamental mechanistic shift: in the absence of photolysis, the primary OH initiation pathway is alkene ozonolysis, which is simultaneously the sole sCI formation pathway. Perturbations to precursors therefore affect both oxidation pathways in the same direction and with similar magnitude, suppressing the conditional interactions that characterize the daytime sensitivity structure. This finding is broadly consistent with previous studies demonstrating that Criegee intermediate chemistry constitutes a non-negligible OH source under dark or low-light conditions (Khan et al., 2018). The rise of RH from a minor factor during the day to the second-ranked control at night reflects the substantially lower OH concentrations characteristic of nocturnal conditions, which elevate the relative contribution of sCIs to gas-phase SO_2 oxidation (Kukui et al., 2021) and thereby amplify the suppressive effect of $H_2O/(H_2O)_2$ on μ_{sCIs}. The contrasting behavior of NO_x and NO_2 % between day and night also warrants attention. At night, photolytic regeneration of NO from NO_2 is effectively absent; instead, NO within NO_x is oxidized to NO_2 through reactions with O_3 and peroxy radicals, leading to progressive NO_2 accumulation. This enhances the termination reaction between NO_2 and OH, suppressing steady-state OH and indirectly elevating μ_{sCIs}. As a result, nighttime μ_{sCIs} is governed primarily by total NO_x abundance rather than by the NO/NO_2 partitioning, which explains why NO_2 % exerts a negligible effect at night.

The directional effects of these features are further elucidated by the 2D PDPs (Fig. 7b–i). ARI, O_3, VOCs, and alkene % exhibit mutually reinforcing positive effects on μ_{sCIs}, consistent with their roles as sCI precursors: conditions favorable for $L_{SO_2,sCIs}$ simultaneously enhance the relative competitiveness of the sCI oxidation pathway. RH exerts a pronounced negative effect on μ_{sCIs}. With respect to NO_x, μ_{sCIs} reaches a locally elevated value (approximately 0.1) at the lowest NO_x level, then drops sharply as NO_x increases only slightly from its minimum, before rising significantly and monotonically across the remainder of the range to reach its global maximum (approximately 0.16) at the highest NO_x level, such that a strong positive relationship between NO_x and μ_{sCIs} prevails across most of the range. This near-monotonic behavior reflects the role of NO_x in modulat-

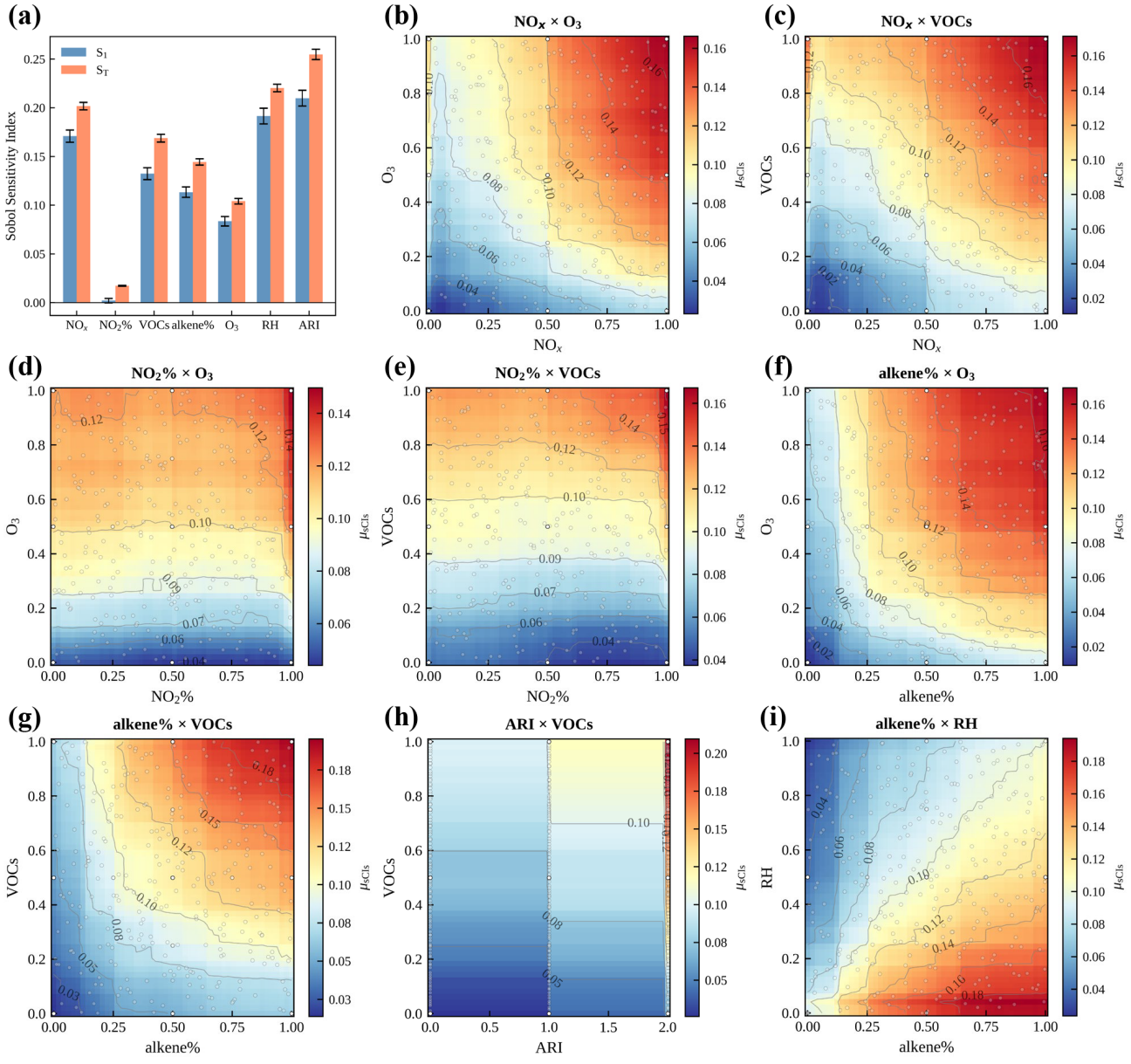

Figure 7. **(a)** First-order (S_1) and total-order (S_T) Sobol sensitivity indices for the seven input features in the XGBoost surrogate model of μ_{sCIs} during nighttime. S_1 quantifies the main effect of each feature acting alone, whereas S_T includes both the main effect and all interaction effects involving that feature. The difference between S_T and S_1 therefore reflects the extent to which a feature participates in non-additive interactions. **(b–i)** Two-dimensional partial dependence plots showing the joint effect of O_3norm×NO_xnorm, VOCsnorm×NO_xnorm, O_3norm×NO_2 %norm, VOCsnorm×NO_2 %norm, O_3norm×alkene %norm, VOCsnorm×alkene %norm, VOCsnorm×ARIcode, and RHnorm×alkene %norm on the surrogate-model prediction of μ_{sCIs} during nighttime. The surface represents the average model response after marginalizing over the remaining features. Warmer colors indicate larger predicted μ_{sCIs}.

ing steady-state OH through radical termination, as described above.

Taken together, nighttime μ_{sCIs} tends to be elevated under atmospheric conditions characterized by high O_3 concentrations, abundant VOCs, a large alkene fraction, and relatively low RH. With respect to NO_x, the highest μ_{sCIs} values occur under elevated NO_x levels, although a smaller enhancement is also evident under extremely low NO_x conditions. This is consistent with a previous study reporting that elevated NO_x levels in power plant environments at night are highly conducive to a large sCI contribution fraction (Meidan et al., 2019). Furthermore, ARI, O_3, VOCs, and alkene %, which collectively characterize conditions favorable for sCI formation, not only strongly promote $L_{SO_2,sCIs}$ but also exert pro-

nounced synergistic effects on μ_{sCIs}. This pattern indicates that O_3 and alkenes do not affect the OH- and sCI-mediated SO_2 oxidation pathways to the same extent. Notably, unlike during the day, when OH is sustained primarily by radical propagation, nocturnal OH production is more strongly linked to primary initiation, alkene ozonolysis, because the absence of photolysis limits OH production from photolytic sources and radical recycling. Alkene ozonolysis is also the sole formation pathway for sCIs. Therefore, differences in the sensitivity of L_{SO_2} across μ_{sCIs} regimes are expected to reflect differences in the strength of the alkene ozonolysis pathway. To examine these differences, the dataset was partitioned into high- and low-μ_{sCIs} subsets based on the median nighttime μ_{sCIs} value (8.0 %), and the relationship between each feature and L_{SO_2} was characterized separately for each subset.

Figure 8 shows how L_{SO_2} responds to precursor perturbations across the high-μ_{sCIs} and low-μ_{sCIs} regimes at night. The mean ICE curves reveal that L_{SO_2} increases monotonically with all three features under both regimes; however, the response is systematically enhanced under the high-μ_{sCIs} regime, with the mean curve exhibiting a steeper and more sustained increase across the full feature range. Beyond the mean response, the spread of individual ICE curves provides insight into response heterogeneity across different atmospheric conditions. For O_3, near-universal positive associations with L_{SO_2} are observed in both regimes, with neg-slope fractions of 1 % and 3 % under the high- and low-μ_{sCIs} regimes, respectively, indicating that O_3 consistently promotes L_{SO_2} regardless of the μ_{sCIs} regime. For alkene %, the neg-slope fraction increases from 1 % under the high-μ_{sCIs} regime to 10 % under the low-μ_{sCIs} regime. The contrast is most pronounced for VOCs, for which the neg-slope fraction rises from 5 % under the high-μ_{sCIs} regime to 29 % under the low-μ_{sCIs} regime, with the excess negative responses in the low-μ_{sCIs} regime arising predominantly from high-NO_x scenarios.

To elucidate the role of alkene ozonolysis in driving these response differences, we examined the OH and sCI budgets for two representative high-NO_x scenarios corresponding to the low-μ_{sCIs} ($\mu_{sCIs} = 0.008$) and high-μ_{sCIs} ($\mu_{sCIs} = 0.14$) regimes, respectively (Fig. 9a, b). Under the low-μ_{sCIs} scenario, alkene ozonolysis accounts for 30.18 % of $\sum OH_{new}$, which is 5.56×10^5 molec. cm^{-3} s^{-1}. In contrast, under the high-μ_{sCIs} scenario, alkene ozonolysis contributes 94.24 % of $\sum OH_{new}$, which reaches 2.29×10^7 molec. cm^{-3} s^{-1}. These results show that, when alkene ozonolysis is efficient at night, it acts not only as the sole formation pathway for sCIs but also as the dominant OH initiation pathway. When alkene ozonolysis is weak, the ratio $OH_{propag}/\sum OH_{new}$ is 16.23, indicating that OH is sustained predominantly through radical cycling. In this regime, OH initiation is supplied primarily by photolysis in the early morning hours, with a smaller contribution from ozonolysis. Reducing total VOCs does not affect the photolytic OH initiation source, but decreases the OH–to–RO_2 flux and thus weakens OH loss through VOC oxidation. Provided that radical recycling efficiency changes little, this reduction in OH reactivity can slightly increase steady-state OH and $L_{SO_2,OH}$. Because the alkene-derived sCI flux is negligible in this regime, $\Delta L_{SO_2,sCIs}$ is close to zero. The OH-mediated response can therefore dominate, producing a net increase in L_{SO_2} as VOCs decrease (a negative slope). Conversely, when alkene ozonolysis is strong, it simultaneously serves as the dominant OH initiation source and the principal sCI formation pathway. The ratio $OH_{propag}/\sum OH_{new}$ decreases to 2.68, far below that under weak ozonolysis, indicating a much greater relative contribution of initiation to OH. Under these conditions, VOC perturbations influence the OH- and sCI-mediated SO_2 oxidation pathways in the same direction, thereby reducing the occurrence of negative L_{SO_2} responses. Between the two scenarios, the rates of ozonolysis-driven sCI and OH formation increase by factors of 127.5 and 123.3, respectively. Accordingly, the rate at which sCIs form H_2SO_4 increases by a factor of 133, whereas the rate at which OH forms H_2SO_4 increases by only a factor of six. This difference arises because OH reacts with alkenes and is incorporated into the RO_x cycle, such that part of the additional OH production supports radical cycling rather than directly increasing steady-state OH. The contrasting neg-slope fractions for VOCs and alkene % can thus be explained by their distinct chemical roles. Reducing alkene % simultaneously weakens a primary OH initiation source and the sCI formation pathway, such that L_{SO_2} declines almost universally. By contrast, reducing total VOCs primarily lowers OH reactivity rather than suppressing OH initiation under alkene-poor conditions corresponding to the low-μ_{sCIs} regime. The resulting increase in OH-mediated oxidation can outweigh the negligible change in the sCI pathway, producing a negative L_{SO_2} response (neg-slope = 29 %).

3.3 Observational–model corroboration for regime-dependent sensitivities of SO_2 oxidation

To validate the predictive capability of the surrogate model developed in Sect. 3.2 for μ_{sCIs}, and to evaluate how the sensitivity of SO_2 oxidation to its precursors depends on the relative contributions of sCIs in ambient air, we selected a summer episode in Wuhai City as a real-atmosphere validation case. Figure 10 presents the constrained simulation results derived from AtChem–MCM v3.3.1, including time series of sulfuric acid concentrations (H_2SO_4–AtChem) and the daytime- and nighttime-averaged fractional contributions of sCIs to total SO_2 oxidation (μ_{sCIs}–AtChem) over the period 1 June to 15 July 2021. The corresponding pollutant mixing ratios and meteorological parameters are shown in Fig. S3. SO_4^{2-} denotes the ambient particulate sulfate mass concentrations measured concurrently by online ion chromatography. The term "μ_{sCIs}–surrogate model" represents the daytime- and nighttime-averaged μ_{sCIs} predictions gen-

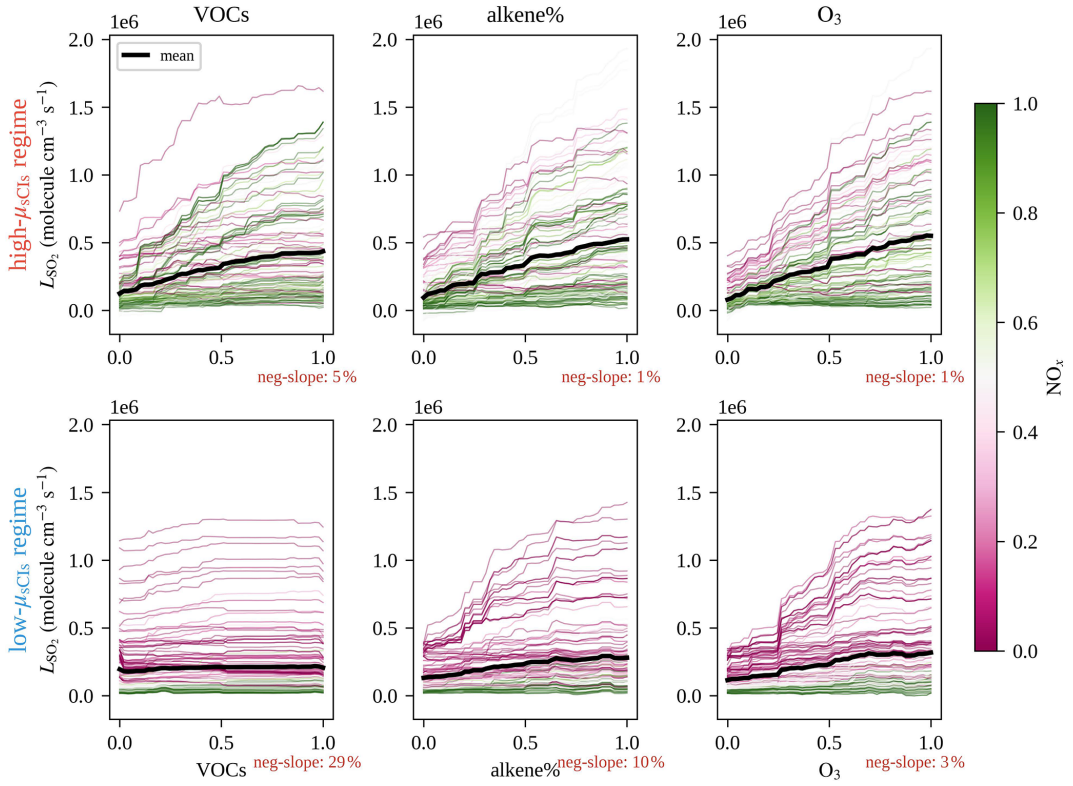

Figure 8. Individual conditional expectation (ICE) plots for the regime-specific L_{SO_2} models during nighttime, showing the responses of predicted total gas-phase SO_2 oxidation to VOCsnorm, alkene %norm, and O_3norm in the low- and high-μ_{sCIs} regimes. The two rows correspond to the two μ_{sCIs} regimes, and the three columns correspond to the three selected predictors. Each thin curve represents one sampled scenario, colored by normalized NO_x. The curves are displayed in absolute prediction space (i.e. without centering), so both the slope and vertical spread reflect heterogeneity in the conditional model responses across different chemical backgrounds.

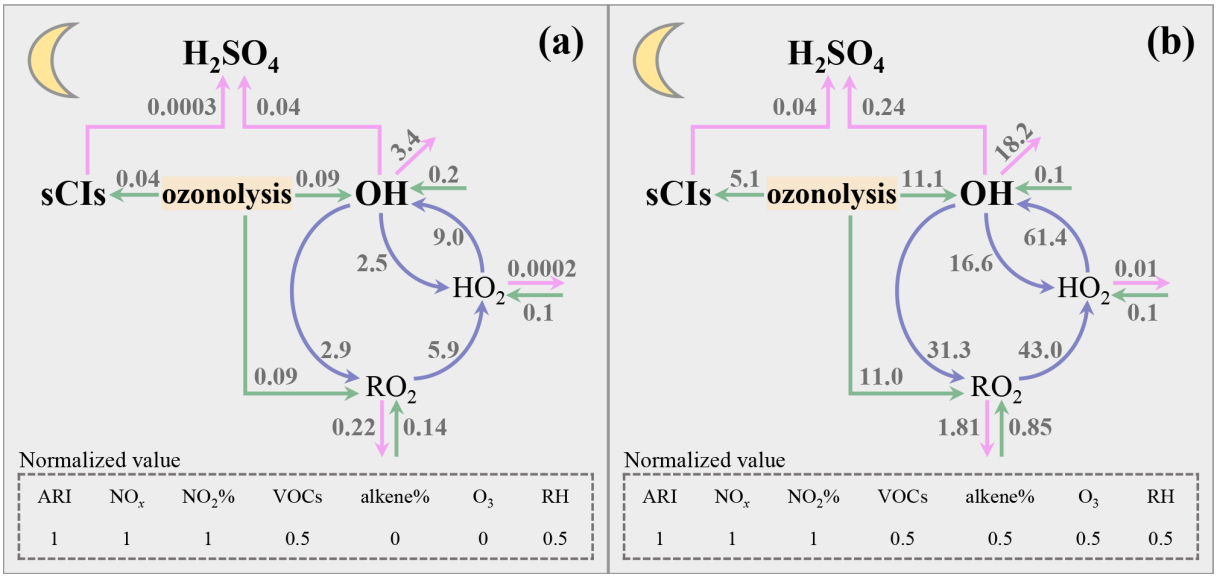

Figure 9. Two representative nighttime scenarios illustrating the budgets of OH and sCIs corresponding to **(a)** the low-μ_{sCIs} regime ($\mu_{sCIs} = 0.008$) and **(b)** the high-μ_{sCIs} regime ($\mu_{sCIs} = 0.14$). Numbers denote reaction rates (10^6 molec. cm^{-3} s^{-1}). Pink, green, and purple lines indicate the termination, initiation, and propagation pathways of OH and sCIs, respectively.

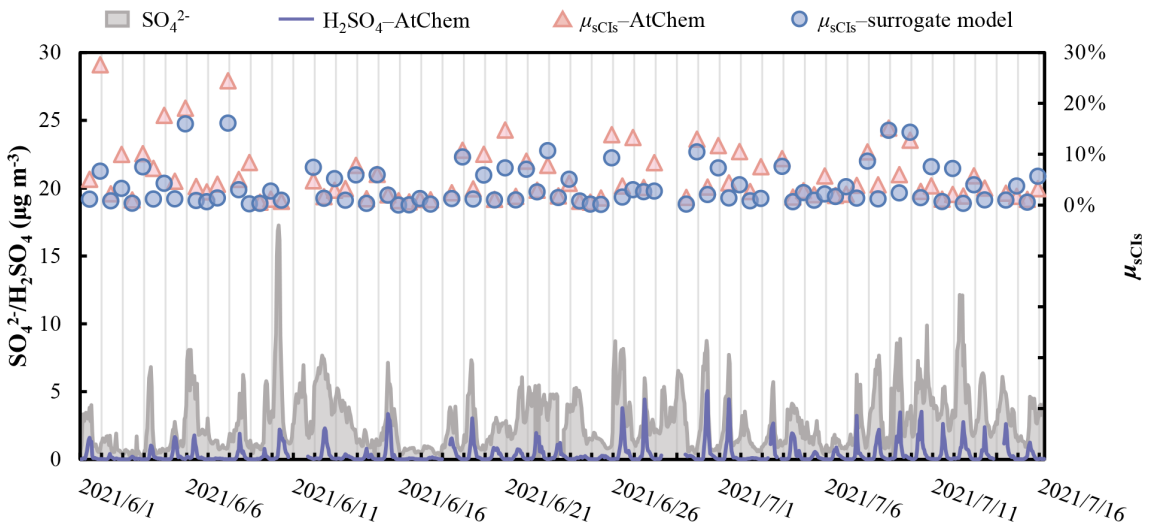

Figure 10. Constrained AtChem–MCM v3.3.1 simulations for a summer episode in Wuhai City (1 June–15 July 2021), showing time series of H_2SO_4–AtChem (AtChem-simulated sulfuric acid concentration), μ_{sCIs}–AtChem (AtChem-simulated fractional contribution of sCIs to total SO_2 oxidation), SO_4^{2-} (concurrently measured ambient particulate sulfate mass concentration), and μ_{sCIs}-surrogate model (daytime- and nighttime-averaged μ_{sCIs} predicted by the surrogate model).

erated by the surrogate model described in Sect. 3.2. The strong agreement ($R^2 = 0.75$) between the surrogate predictions (μ_{sCIs}–surrogate model) and the explicit AtChem simulations (μ_{sCIs}–AtChem) demonstrates the robust predictive performance of the constructed machine learning surrogate for μ_{sCIs}.

To evaluate whether ambient SO_4^{2-} concentrations serve as a reliable proxy for gas-phase H_2SO_4 production during the target episode, an XGBoost model was trained on a comprehensive long-term observational dataset spanning 9 October 2019 to 30 June 2022 (summary statistics of all variables are provided in Table S4), with hourly SO_4^{2-} concentration as the target variable. The feature set included $PM_{2.5}$, NO_3^-, SO_2, O_3, VOCs, alkene %, NO_x, NO_2 %, RH, wind speed (WS), and Fe. Training over this extended period ensures that the model captures the full range of variability in sulfate formation, including seasonal cycles, episodic pollution events, and varying meteorological regimes, thereby establishing a representative and well-generalized mapping between precursor conditions and SO_4^{2-}. SHAP values were then extracted exclusively for the target episode (1 June to 15 July 2021) to attribute feature contributions during this specific period. As shown in Fig. 11a, the three highest-ranked features are NO_3^-, SO_2, and $PM_{2.5}$, all of which exhibit clear positive correlations with SO_4^{2-}. The elevated NO_3^- co-occurs with SO_4^{2-}, together with the concurrent increase in $PM_{2.5}$, consistent with the hallmark of secondary inorganic aerosol formation (Gao et al., 2021). The strong positive SHAP contribution of SO_2 directly corroborates its role as the primary precursor for SO_4^{2-} production. Notably, WS also exerts a discernible positive contribution, suggesting a degree of regional transport influence during this episode, although its impact remains secondary to in situ chemical production. By contrast, RH shows no significant positive correlation with SO_4^{2-} and ranks relatively low in feature importance. Fe, a key catalyst for aqueous-phase SO_2 oxidation via Fenton-type chemistry (Ye et al., 2023), shows no clear positive association with SO_4^{2-}, with elevated ambient Fe concentrations not corresponding to enhanced sulfate formation. Taken together, these results indicate that aqueous-phase oxidation was not the dominant SO_4^{2-} formation pathway during the target episode. Meanwhile, O_3, VOCs, and alkene %, which serve as key proxies of gas-phase oxidant pathways, exhibit positive correlations with SO_4^{2-}, providing evidence that gas-phase oxidation constituted the primary sulfate formation pathway during this period. On this basis, ambient SO_4^{2-} concentrations can be regarded as a reliable observational proxy for the variability in total gas-phase H_2SO_4 production during the target episode.

To further examine whether the sensitivity of SO_4^{2-} to key precursors is consistent with the regime-dependent behavior of L_{SO_2} identified in Sect. 3.2, the target episode was partitioned into high- and low-μ_{sCIs} subsets for daytime and nighttime periods separately, using the same classification thresholds applied in Sect. 3.2 (daytime: 1.1 %; nighttime: 8.0 %). SHAP values for O_3, VOCs, and alkene % were extracted for each subset and compared. During the daytime (Fig. 11b), the high-μ_{sCIs} subset exhibits systematically amplified SHAP responses relative to the low-μ_{sCIs} subset across all three features. O_3 shows the most pronounced regime contrast: in the high-μ_{sCIs} subset, high feature values (red) are associated with distinctly larger positive SHAP contributions and a considerably wider spread, whereas the corresponding responses in the low-μ_{sCIs} sub-

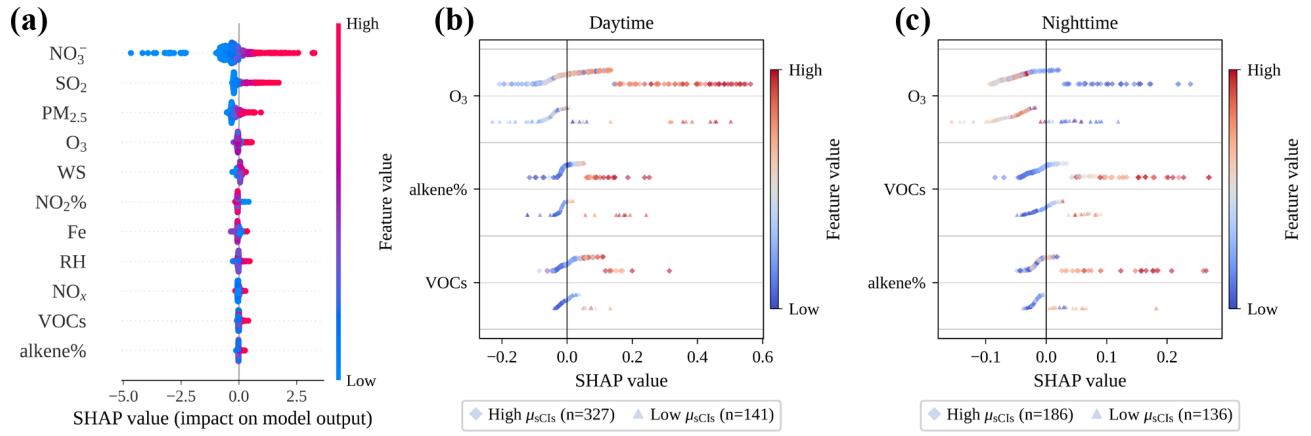

Figure 11. **(a)** SHAP beeswarm summary plot for the observation-based XGBoost model of ambient SO_4^{2-}. Each point represents one hourly observation, positioned according to the SHAP value of the corresponding predictor. Positive SHAP values indicate that the predictor increases the model-predicted SO_4^{2-} concentration, whereas negative values indicate a suppressing effect. Point colour denotes the predictor magnitude from low to high. Features are ordered by mean absolute SHAP value, so the plot summarizes both the relative importance and the directionality of the physically interpretable features. **(b)** Comparison of SHAP beeswarm plots for the observation-based XGBoost model under daytime low- and high-μ_{sCIs} regimes. Each point represents one hourly observation in the corresponding subset. The horizontal position gives the SHAP value, and the color indicates the feature value. Differences between the two panels illustrate how the relative importance and directional effects of observed predictors on ambient SO_4^{2-} vary between daytime chemical regimes with low and high inferred sCI contributions. **(c)** Comparison of SHAP beeswarm plots for the observation-based XGBoost model under nighttime low- and high-μ_{sCIs} regimes. Each point represents one hourly observation in the corresponding subset. The horizontal position gives the SHAP value, and the color indicates the feature value. Differences between the two panels illustrate how the relative importance and directional effects of observed predictors on ambient SO_4^{2-} vary between nighttime chemical regimes with low and high inferred sCI contributions.

set are substantially attenuated. VOCs and alkene % follow the same pattern, with high feature values driving larger positive SHAP contributions under high-μ_{sCIs} conditions. This daytime regime contrast is consistent with the finding in Sect. 3.2 that the sensitivity of SO_2 oxidation to O_3, VOCs, and alkene % is amplified under high-μ_{sCIs} conditions, providing observational corroboration of that mechanistic result. At night (Fig. 11c), VOCs and alkene % exhibit stronger positive SHAP contributions to SO_4^{2-} in the high-μ_{sCIs} subset, consistent with their roles in promoting both sCIs and OH formation through nocturnal alkene ozonolysis. By contrast, O_3 exhibits negative SHAP contributions in both subsets, which can be attributed to the distinct behavior of O_3 at night: nocturnal O_3 is primarily of advective origin rather than in situ photochemical production, and elevated O_3 concentrations are often associated with suppressed local NO levels due to rapid O_3–NO titration. Taken together, the regime-dependent SO_4^{2-} sensitivity patterns observed during the target episode (Fig. 11b, c) provide observational validation for the mechanistic findings derived from the AtChem-based surrogate model simulations in Sect. 3.2, confirming that these findings are manifested in ambient atmospheric measurements. This cross-validation between model-diagnosed sensitivity and observation-based attribution reinforces the conclusion that under high-μ_{sCIs} regimes, alkene-targeted emission control strategies can effectively reduce sCIs and suppress the total SO_2 oxidation rate, while rarely triggering a rebound in OH-driven oxidation pathways.

4 Summary and conclusion

Sulfuric acid plays a central role in atmospheric aerosol formation, yet effective mitigation requires quantifying the sensitivity of H_2SO_4 formation to its precursors, which varies across atmospheric conditions as the relative contributions of different gas-phase SO_2 oxidation pathways shift. By treating sCIs as reactive intermediate species linking precursor emissions to H_2SO_4 formation, this study deploys an interpretable multi-target XGBoost modeling framework trained on ensemble box-model simulations incorporating updated CI chemistry. This framework determines the controls on sCI-mediated SO_2 oxidation ($L_{SO_2,sCIs}$) and on the fractional sCI contribution (μ_{sCIs}), while establishing how the regime of μ_{sCIs} itself reshapes the sensitivity of total SO_2 oxidation (L_{SO_2}) to its precursors.

$L_{SO_2,sCIs}$ is dominated by RH (29.5 %) and isoprene (23.8 %), revealing that low humidity and high biogenic emissions primarily promote the sCI-mediated oxidation pathways. For μ_{sCIs}, the dominant controlling factors exhibit a pronounced diurnal shift: daytime control resides in alkene reactivity (ARI), O_3, alkene fraction, and total VOCs, whereas nighttime control transitions to ARI, RH, and NO_x. High-μ_{sCIs} regimes uniformly amplify positive L_{SO_2} sensi-

tivities to O_3, VOCs, and alkene %, while decreasing the frequency of occasional negative L_{SO_2} responses to VOCs or alkene %. Observation-based modeling of a Wuhai summer episode with SHAP-based attribution of ambient sulfate provided support for this regime dependence.

Previous studies have extensively reported the contribution of the SO_2 + sCI reaction to total sCI loss (Cox et al., 2020), and the contribution of sCIs to overall SO_2 oxidation across diverse atmospheric conditions (Khan et al., 2018). Building on the understanding that sCI chemistry constitutes one pathway for SO_2 oxidation and that sCIs are secondarily formed atmospheric intermediates, this study no longer treats them as terminal oxidants but rather takes seriously their role as an intermediate species and establishes quantitative relationships linking controlling factors to both the sCI-mediated SO_2 oxidation rate and its fractional contribution to total SO_2 oxidation. The resulting picture goes beyond estimating the sCI contribution for an individual scenario, extending instead to a predictive understanding of the role sCIs may play across a wider range of atmospheric conditions. By further analyzing how the sensitivity of total SO_2 oxidation to factor perturbations varies among internal oxidation regimes characterized by different μ_{sCIs} values, this work provides a scientific basis for developing strategies to mitigate H_2SO_4 formation. Beyond these mechanistic-sensitivity insights, the interpretable surrogate modeling framework developed here offers a transferable approach for distilling quantitative relationships between reactants and products from complex reaction networks. By linking targeted box-model scenario design to machine-learning-based sensitivity diagnostics, this methodology enables efficient identification of dominant kinetic controls – providing a basis for prioritizing kinetic processes for explicit representation when developing lumped chemical mechanisms for chemical transport models.

It should be noted that applying these findings to real-world atmospheric phenomena requires recognizing specific applicability conditions. While key feature variables were explicitly modeled, capturing full atmospheric variability also requires future integration of transport, deposition, multiphase processes, temperature dependence, and other factors. Additionally, our 100 % SO_3 yield assumption for the sCI + SO_2 reaction establishes an upper bound for absolute sCI-mediated H_2SO_4 production and fractional contributions. Because this yield functions as a linear scaling factor, absolute magnitudes may be overestimated, but the underlying functional relationships between controlling factors and sCI chemistry remain unchanged.

Data availability. The dataset supporting the findings of this study is publicly available from Zenodo (Zhu, 2026) at https://doi.org/10.5281/zenodo.21969205.

Supplement. The supplement related to this article is available online at https://doi.org/10.5194/acp-26-12479-2026-supplement.

Author contributions. YZ developed the methodology, performed data curation, visualization, formal analysis, and wrote the original draft. QC conceptualized the study, contributed to formal analysis, acquired funding, and reviewed and edited the manuscript. LH and WG participated in the revision of the manuscript. CS, DG, LJ, and GY contributed to data curation.

Competing interests. The contact author has declared that none of the authors has any competing interests.

Disclaimer. Publisher's note: Copernicus Publications remains neutral with regard to jurisdictional claims made in the text, published maps, institutional affiliations, or any other geographical representation in this paper. The authors bear the ultimate responsibility for providing appropriate place names. Views expressed in the text are those of the authors and do not necessarily reflect the views of the publisher.

Acknowledgements. We thank the editors and anonymous reviewers for their valuable comments on the manuscript. During the preparation of this work, we used ChatGPT to proofread and refine the English expression of the manuscript. This included correcting grammatical errors, enhancing clarity, and improving the overall flow and coherence of the text. After using this tool, we reviewed and edited the content and take full responsibility for the content of the published article.

Financial support. This research has been supported by the Lanzhou Science and Technology Bureau (project no. 2022-2-15) and the National Natural Science Foundation of China (grant no. 42305118).

Review statement. This paper was edited by Lisa Whalley and reviewed by two anonymous referees.

References

Boy, M., Mogensen, D., Smolander, S., Zhou, L., Nieminen, T., Paasonen, P., Plass-Dülmer, C., Sipilä, M., Petäjä, T., Mauldin, L., Berresheim, H., and Kulmala, M.: Oxidation of SO_2 by stabilized Criegee intermediate (sCI) radicals as a crucial source for atmospheric sulfuric acid concentrations, Atmos. Chem. Phys., 13, 3865–3879, https://doi.org/10.5194/acp-13-3865-2013, 2013.

Cao, J., Qiu, X., Gao, J., Wang, F., Wang, J., Wu, J., and Peng, L.: Significant decrease in SO_2 emission and enhanced atmospheric oxidation trigger changes in sulfate formation pathways in China during 2008–2016, J. Clean. Prod., 326, 129396, https://doi.org/10.1016/j.jclepro.2021.129396, 2021.

Cao, J., Zheng, B., Chen, J., and Liu, Y.: Assessment of sulfate and nitrate variations in China during 1990–2020: Insights into source contributions and formation pathways, J. Hazard. Mater., 489, 137600, https://doi.org/10.1016/j.jhazmat.2025.137600, 2025.

Chen, T. and Guestrin, C.: XGBoost: A Scalable Tree Boosting System, in: Proceedings of the 22nd ACM SIGKDD International Conference on Knowledge Discovery and Data Mining, KDD '16: The 22nd ACM SIGKDD International Conference on Knowledge Discovery and Data Mining, San Francisco California USA, 785–794, https://doi.org/10.1145/2939672.2939785, 2016.

Cox, R. A. and Penkett, S. A.: Oxidation of Atmospheric SO_2 by Products of the Ozone–Olefin Reaction, Nature, 230, 321–322, https://doi.org/10.1038/230321a0, 1971.

Cox, R. A., Ammann, M., Crowley, J. N., Herrmann, H., Jenkin, M. E., McNeill, V. F., Mellouki, A., Troe, J., and Wallington, T. J.: Evaluated kinetic and photochemical data for atmospheric chemistry: Volume VII – Criegee intermediates, Atmos. Chem. Phys., 20, 13497–13519, https://doi.org/10.5194/acp-20-13497-2020, 2020.

Dada, L., Ylivinkka, I., Baalbaki, R., Li, C., Guo, Y., Yan, C., Yao, L., Sarnela, N., Jokinen, T., Daellenbach, K. R., Yin, R., Deng, C., Chu, B., Nieminen, T., Wang, Y., Lin, Z., Thakur, R. C., Kontkanen, J., Stolzenburg, D., Sipilä, M., Hussein, T., Paasonen, P., Bianchi, F., Salma, I., Weidinger, T., Pikridas, M., Sciare, J., Jiang, J., Liu, Y., Petäjä, T., Kerminen, V.-M., and Kulmala, M.: Sources and sinks driving sulfuric acid concentrations in contrasting environments: implications on proxy calculations, Atmos. Chem. Phys., 20, 11747–11766, https://doi.org/10.5194/acp-20-11747-2020, 2020.

Dai, Q., Bi, X., Song, W., Li, T., Liu, B., Ding, J., Xu, J., Song, C., Yang, N., Schulze, B. C., Zhang, Y., Feng, Y., and Hopke, P. K.: Residential coal combustion as a source of primary sulfate in Xi'an, China, Atmos. Environ., 196, 66–76, https://doi.org/10.1016/j.atmosenv.2018.10.002, 2019.

Friedman, J. H.: Greedy function approximation: A gradient boosting machine, Ann. Stat., 29, 1189–1232, https://doi.org/10.1214/aos/1013203451, 2001.

Gao, J., Li, Y., Li, J., Shi, G., Liu, Z., Han, B., Tian, X., Wang, Y., Feng, Y., and Russell, A. G.: Impact of Formation Pathways on Secondary Inorganic Aerosol During Haze Pollution in Beijing: Quantitative Evidence From High-Resolution Observation and Modeling, Geophys. Res. Lett., 48, e2021GL095623, https://doi.org/10.1029/2021GL095623, 2021.

Geng, G., Zheng, Y., Zhang, Q., Xue, T., Zhao, H., Tong, D., Zheng, B., Li, M., Liu, F., Hong, C., He, K., and Davis, S. J.: Drivers of $PM_{2.5}$ air pollution deaths in China 2002–2017, Nat. Geosci., 14, 645–650, https://doi.org/10.1038/s41561-021-00792-3, 2021.

Giorio, C., Doussin, J., D'Anna, B., Mas, S., Filippi, D., Denjean, C., Mallet, M. D., Bourrianne, T., Burnet, F., Cazaunau, M., Chikwililwa, C., Desboeufs, K., Feron, A., Michoud, V., Namwoonde, A., Andreae, M. O., Piketh, S. J., and Formenti, P.: Butene Emissions From Coastal Ecosystems May Contribute to New Particle Formation, Geophys. Res. Lett., 49, e2022GL098770, https://doi.org/10.1029/2022GL098770, 2022.

Goldstein, A., Kapelner, A., Bleich, J., and Pitkin, E.: Peeking Inside the Black Box: Visualizing Statistical Learning With Plots of Individual Conditional Expectation, J. Comput. Graph. Stat., 24, 44–65, https://doi.org/10.1080/10618600.2014.907095, 2015.

Gunthe, S. S., Rose, D., Su, H., Garland, R. M., Achtert, P., Nowak, A., Wiedensohler, A., Kuwata, M., Takegawa, N., Kondo, Y., Hu, M., Shao, M., Zhu, T., Andreae, M. O., and Pöschl, U.: Cloud condensation nuclei (CCN) from fresh and aged air pollution in the megacity region of Beijing, Atmos. Chem. Phys., 11, 11023–11039, https://doi.org/10.5194/acp-11-11023-2011, 2011.

Guo, W., Yang, Y., Chen, Q., Zhu, Y., Zhang, Y., Zhang, Y., Liu, Y., Li, G., Sun, W., and She, J.: Chemical reactivity of volatile organic compounds and their effects on ozone formation in a petrochemical industrial area of Lanzhou, Western China, Sci. Total Environ., 839, 155901, https://doi.org/10.1016/j.scitotenv.2022.155901, 2022.

Guo, Y., Yan, C., Li, C., Ma, W., Feng, Z., Zhou, Y., Lin, Z., Dada, L., Stolzenburg, D., Yin, R., Kontkanen, J., Daellenbach, K. R., Kangasluoma, J., Yao, L., Chu, B., Wang, Y., Cai, R., Bianchi, F., Liu, Y., and Kulmala, M.: Formation of nighttime sulfuric acid from the ozonolysis of alkenes in Beijing, Atmos. Chem. Phys., 21, 5499–5511, https://doi.org/10.5194/acp-21-5499-2021, 2021.

Hata, H., Hoshino, S., Fujita, M., and Tonokura, K.: Atmospheric impact of isoprene-derived Criegee intermediates and isoprene hydroxy hydroperoxide on sulfate aerosol formation in the Asian region, Atmos. Environ., 20, 100226, https://doi.org/10.1016/j.aeaoa.2023.100226, 2023.

Herman, J. and Usher, W.: SALib: An open-source Python library for Sensitivity Analysis, JOSS, 2, 97, https://doi.org/10.21105/joss.00097, 2017.

Jenkin, M. E., Saunders, S. M., and Pilling, M. J.: The tropospheric degradation of volatile organic compounds: a protocol for mechanism development, Atmos. Environ., 31, 81–104, https://doi.org/10.1016/S1352-2310(96)00105-7, 1997.

Jenkin, M. E., Young, J. C., and Rickard, A. R.: The MCM v3.3.1 degradation scheme for isoprene, Atmos. Chem. Phys., 15, 11433–11459, https://doi.org/10.5194/acp-15-11433-2015, 2015.

Khan, M. A. H., Morris, W. C., Galloway, M., Shallcross, B. M. A., Percival, C. J., and Shallcross, D. E.: An Estimation of the Levels of Stabilized Criegee Intermediates in the UK Urban and Rural Atmosphere Using the Steady-State Approximation and the Potential Effects of These Intermediates on Tropospheric Oxidation Cycles, Int. J. Chem. Kinet., 49, 611–621, https://doi.org/10.1002/kin.21101, 2017.

Khan, M. A. H., Percival, C. J., Caravan, R. L., Taatjes, C. A., and Shallcross, D. E.: Criegee intermediates and their impacts on the troposphere, Environ. Sci.: Processes Impacts, 20, 437–453, https://doi.org/10.1039/C7EM00585G, 2018.

Kim, S., Guenther, A., Lefer, B., Flynn, J., Griffin, R., Rutter, A. P., Gong, L., and Cevik, B. K.: Potential Role of Stabilized Criegee Radicals in Sulfuric Acid Production in a High Biogenic VOC Environment, Environ. Sci. Technol., 49, 3383–3391, https://doi.org/10.1021/es505793t, 2015.

Kukui, A., Chartier, M., Wang, J., Chen, H., Dusanter, S., Sauvage, S., Michoud, V., Locoge, N., Gros, V., Bourrianne, T., Sellegri, K., and Pichon, J.-M.: Role of Criegee intermediates in the formation of sulfuric acid at a Mediterranean (Cape Corsica) site under influence of biogenic emissions, Atmos. Chem.

Phys., 21, 13333–13351, https://doi.org/10.5194/acp-21-13333-2021, 2021.

Lade, R. E., Blitz, M. A., Rowlinson, M., Evans, M. J., Seakins, P. W., and Stone, D.: Kinetics of the reactions of the Criegee intermediate CH_2OO with water vapour: experimental measurements as a function of temperature and global atmospheric modelling, Environ. Sci.: Atmos., 4, 1294–1308, https://doi.org/10.1039/D4EA00097H, 2024.

Li, J., Ying, Q., Yi, B., and Yang, P.: Role of stabilized Criegee Intermediates in the formation of atmospheric sulfate in eastern United States, Atmos. Environ., 79, 442–447, https://doi.org/10.1016/j.atmosenv.2013.06.048, 2013.

Lu, K., Guo, S., Tan, Z., Wang, H., Shang, D., Liu, Y., Li, X., Wu, Z., Hu, M., and Zhang, Y.: Exploring atmospheric free-radical chemistry in China: the self-cleansing capacity and the formation of secondary air pollution, Natl. Sci. Rev., 6, 579–594, https://doi.org/10.1093/nsr/nwy073, 2019.

Lundberg, S. M. and Lee, S.-I.: A Unified Approach to Interpreting Model Predictions, Neural Inf. Process. Syst., arXiv [preprint], https://doi.org/10.48550/arXiv.1705.07874, 2017.

Lundberg, S. M., Nair, B., Vavilala, M. S., Horibe, M., Eisses, M. J., Adams, T., Liston, D. E., Low, D. K.-W., Newman, S.-F., Kim, J., and Lee, S.-I.: Explainable machine-learning predictions for the prevention of hypoxaemia during surgery, Nat. Biomed. Eng., 2, 749–760, https://doi.org/10.1038/s41551-018-0304-0, 2018.

Lundberg, S. M., Erion, G. G., and Lee, S.-I.: Consistent Individualized Feature Attribution for Tree Ensembles, arXiv [preprint], https://doi.org/10.48550/arXiv.1802.03888, 7 March 2019.

Lundberg, S. M., Erion, G., Chen, H., DeGrave, A., Prutkin, J. M., Nair, B., Katz, R., Himmelfarb, J., Bansal, N., and Lee, S.-I.: From local explanations to global understanding with explainable AI for trees, Nat. Mach. Intell., 2, 56–67, https://doi.org/10.1038/s42256-019-0138-9, 2020.

Mauldin, R. L., Berndt, T., Sipilä, M., Paasonen, P., Petäjä, T., Kim, S., Kurtén, T., Stratmann, F., Kerminen, V.-M., and Kulmala, M.: A new atmospherically relevant oxidant of sulphur dioxide, Nature, 488, 193–196, https://doi.org/10.1038/nature11278, 2012.

Meidan, D., Holloway, J. S., Edwards, P. M., Dubé, W. P., Middlebrook, A. M., Liao, J., Welti, A., Graus, M., Warneke, C., Ryerson, T. B., Pollack, I. B., Brown, S. S., and Rudich, Y.: Role of Criegee Intermediates in Secondary Sulfate Aerosol Formation in Nocturnal Power Plant Plumes in the Southeast US, ACS Earth and Space Chem., 3, 748–759, https://doi.org/10.1021/acsearthspacechem.8b00215, 2019.

Newland, M. J., Rickard, A. R., Alam, M. S., Vereecken, L., Muñoz, A., Ródenas, M., and Bloss, W. J.: Kinetics of stabilised Criegee intermediates derived from alkene ozonolysis: reactions with SO_2, H_2O and decomposition under boundary layer conditions, Phys. Chem. Chem. Phys., 17, 4076–4088, https://doi.org/10.1039/C4CP04186K, 2015.

Onel, L., Lade, R., Mortiboy, J., Blitz, M. A., Seakins, P. W., Heard, D. E., and Stone, D.: Kinetics of the gas phase reaction of the Criegee intermediate CH_2OO with SO_2 as a function of temperature, Phys. Chem. Chem. Phys., 23, 19415–19423, https://doi.org/10.1039/D1CP02932K, 2021.

Quaas, J., Jia, H., Smith, C., Albright, A. L., Aas, W., Bellouin, N., Boucher, O., Doutriaux-Boucher, M., Forster, P. M., Grosvenor, D., Jenkins, S., Klimont, Z., Loeb, N. G., Ma, X., Naik, V., Paulot, F., Stier, P., Wild, M., Myhre, G., and Schulz, M.: Robust evidence for reversal of the trend in aerosol effective climate forcing, Atmos. Chem. Phys., 22, 12221–12239, https://doi.org/10.5194/acp-22-12221-2022, 2022.

Rhew, R. C., Deventer, M. J., Turnipseed, A. A., Warneke, C., Ortega, J., Shen, S., Martinez, L., Koss, A., Lerner, B. M., Gilman, J. B., Smith, J. N., Guenther, A. B., and de Gouw, J. A.: Ethene, propene, butene and isoprene emissions from a ponderosa pine forest measured by relaxed eddy accumulation, Atmos. Chem. Phys., 17, 13417–13438, https://doi.org/10.5194/acp-17-13417-2017, 2017.

Ruscic, B.: Active Thermochemical Tables: Water and Water Dimer, J. Phys. Chem. A, 117, 11940–11953, https://doi.org/10.1021/jp403197t, 2013.

Saltelli, A.: Making best use of model evaluations to compute sensitivity indices, Comput. Phys. Commun., 145, 280–297, https://doi.org/10.1016/S0010-4655(02)00280-1, 2002.

Saltelli, A., Annoni, P., Azzini, I., Campolongo, F., Ratto, M., and Tarantola, S.: Variance based sensitivity analysis of model output. Design and estimator for the total sensitivity index, Comput. Phys. Commun., 181, 259–270, https://doi.org/10.1016/j.cpc.2009.09.018, 2010.

Sarwar, G., Simon, H., Fahey, K., Mathur, R., Goliff, W. S., and Stockwell, W. R.: Impact of sulfur dioxide oxidation by Stabilized Criegee Intermediate on sulfate, Atmos. Environ., 85, 204–214, https://doi.org/10.1016/j.atmosenv.2013.12.013, 2014.

Saunders, S. M., Jenkin, M. E., Derwent, R. G., and Pilling, M. J.: Protocol for the development of the Master Chemical Mechanism, MCM v3 (Part A): tropospheric degradation of non-aromatic volatile organic compounds, Atmos. Chem. Phys., 3, 161–180, https://doi.org/10.5194/acp-3-161-2003, 2003.

Scribano, Y., Goldman, N., Saykally, R. J., and Leforestier, C.: Water Dimers in the Atmosphere III: Equilibrium Constant from a Flexible Potential, J. Phys. Chem. A, 110, 5411–5419, https://doi.org/10.1021/jp056759k, 2006.

Sheehy, P. M., Volkamer, R., Molina, L. T., and Molina, M. J.: Oxidative capacity of the Mexico City atmosphere – Part 2: A RO_x radical cycling perspective, Atmos. Chem. Phys., 10, 6993–7008, https://doi.org/10.5194/acp-10-6993-2010, 2010.

Sillman, S. and He, D.: Some theoretical results concerning O_3–NO_x–VOC chemistry and NO_x–VOC indicators, J. Geophys. Res.-Atmos., 107, https://doi.org/10.1029/2001JD001123, 2002.

Sobol, I. M.: Global sensitivity indices for nonlinear mathematical models and their Monte Carlo estimates, Math. Comput. Simulat., 55, 271–280, https://doi.org/10.1016/S0378-4754(00)00270-6, 2001.

Sommariva, R., Cox, S., Martin, C., Borońska, K., Young, J., Jimack, P. K., Pilling, M. J., Matthaios, V. N., Nelson, B. S., Newland, M. J., Panagi, M., Bloss, W. J., Monks, P. S., and Rickard, A. R.: AtChem (version 1), an open-source box model for the Master Chemical Mechanism, Geosci. Model Dev., 13, 169–183, https://doi.org/10.5194/gmd-13-169-2020, 2020.

Song, X., Yi, J., Chen, Y., Su, Y., Wang, H., Liu, A., Wu, D., and Li, Q.: Condensable particulate matter emissions regulated by flue gas desulfurization technologies in typical industrial plants, J. Hazard. Mater., 489, 137527, https://doi.org/10.1016/j.jhazmat.2025.137527, 2025.

Taatjes, C. A., Welz, O., Eskola, A. J., Savee, J. D., Scheer, A. M., Shallcross, D. E., Rotavera, B., Lee, E. P. F., Dyke, J. M., Mok, D. K. W., Osborn, D. L., and Percival, C. J.:

Direct Measurements of Conformer-Dependent Reactivity of the Criegee Intermediate CH_3CHOO, Science, 340, 177–180, https://doi.org/10.1126/science.1234689, 2013.

Vereecken, L., Harder, H., and Novelli, A.: The reaction of Criegee intermediates with NO, RO_2, and SO_2, and their fate in the atmosphere, Phys. Chem. Chem. Phys., 14, 14682, https://doi.org/10.1039/c2cp42300f, 2012.

Vereecken, L., Novelli, A., and Taraborrelli, D.: Unimolecular decay strongly limits the atmospheric impact of Criegee intermediates, Phys. Chem. Chem. Phys., 19, 31599–31612, https://doi.org/10.1039/C7CP05541B, 2017.

Wang, Z., Nie, W., Liu, Y., Yang, L., Liu, C., Zhang, Y., Yan, C., Zha, Q., Ge, D., Qi, X., Zhou, C., Chen, L., Zhou, X., Wang, L., Huang, D. D., Chi, X., and Ding, A.: Gaseous Sulfuric Acid Contributions to Sulfate Formation in Urban Atmosphere, Environ. Sci. Technol. Lett., 12, 189–195, https://doi.org/10.1021/acs.estlett.4c01028, 2025.

WHO: WHO Global Air Quality Guidelines: Particulate Matter ($PM_{2.5}$ and PM_{10}), Ozone, Nitrogen Dioxide, Sulfur Dioxide and Carbon Monoxide, 1st edn., World Health Organization, https://iris.who.int/handle/10665/345329 (last access: 31 August 2026), 2021.

Yang, L., Nie, W., Liu, Y., Xu, Z., Xiao, M., Qi, X., Li, Y., Wang, R., Zou, J., Paasonen, P., Yan, C., Xu, Z., Wang, J., Zhou, C., Yuan, J., Sun, J., Chi, X., Kerminen, V.-M., Kulmala, M., and Ding, A.: Toward Building a Physical Proxy for Gas-Phase Sulfuric Acid Concentration Based on Its Budget Analysis in Polluted Yangtze River Delta, East China, Environ. Sci. Technol., 55, 6665–6676, https://doi.org/10.1021/acs.est.1c00738, 2021.

Yao, L., Garmash, O., Bianchi, F., Zheng, J., Yan, C., Kontkanen, J., Junninen, H., Mazon, S. B., Ehn, M., Paasonen, P., Sipilä, M., Wang, M., Wang, X., Xiao, S., Chen, H., Lu, Y., Zhang, B., Wang, D., Fu, Q., Geng, F., Li, L., Wang, H., Qiao, L., Yang, X., Chen, J., Kerminen, V.-M., Petäjä, T., Worsnop, D. R., Kulmala, M., and Wang, L.: Atmospheric new particle formation from sulfuric acid and amines in a Chinese megacity, Science, 361, 278–281, https://doi.org/10.1126/science.aao4839, 2018.

Ye, C., Lu, K., Song, H., Mu, Y., Chen, J., and Zhang, Y.: A critical review of sulfate aerosol formation mechanisms during winter polluted periods, J. Environ. Sci., 123, 387–399, https://doi.org/10.1016/j.jes.2022.07.011, 2023.

Zhao, Q., Bi, J., Liu, Q., Ling, Z., Shen, G., Chen, F., Qiao, Y., Li, C., and Ma, Z.: Sources of volatile organic compounds and policy implications for regional ozone pollution control in an urban location of Nanjing, East China, Atmos. Chem. Phys., 20, 3905–3919, https://doi.org/10.5194/acp-20-3905-2020, 2020.

Zhu, Y.: Data-Revisiting the critical role of stabilized Criegee intermediates (sCIs) in sulfuric acid formation: coupling mechanistic updates with interpretable machine learning, Zenodo [data set], https://doi.org/10.5281/zenodo.21969205, 2026.